# Galaxies that shine: radiation-hydrodynamical simulations of disc galaxies

Joakim Rosdahl,[1]⋆ Joop Schaye,[1] Romain Teyssier[2] and Oscar Agertz[3]

[1]*Leiden Observatory, Leiden University, PO Box 9513, NL-2300 RA Leiden, the Netherlands*
[2]*Institute for Computational Science, University of Zürich, Winterthurerstrasse 190, CH-8057 Zürich, Switzerland*
[3]*Department of Physics, University of Surrey, Guildford, GU2 7XH Surrey, UK*

## ABSTRACT

Radiation feedback is typically implemented using subgrid recipes in hydrodynamical simulations of galaxies. Very little work has so far been performed using radiation-hydrodynamics (RHD), and there is no consensus on the importance of radiation feedback in galaxy evolution. We present RHD simulations of isolated galaxy discs of different masses with a resolution of 18 pc. Besides accounting for supernova feedback, our simulations are the first galaxy-scale simulations to include RHD treatments of photoionization heating and radiation pressure, from both direct optical/UV radiation and multiscattered, re-processed infrared (IR) radiation. Photoheating smooths and thickens the discs and suppresses star formation about as much as the inclusion of ('thermal dump') supernova feedback does. These effects decrease with galaxy mass and are mainly due to the prevention of the formation of dense clouds, as opposed to their destruction. Radiation pressure, whether from direct or IR radiation, has little effect, but for the IR radiation we show that its impact is limited by our inability to resolve the high optical depths for which multiscattering becomes important. While artificially boosting the IR optical depths does reduce the star formation, it does so by smoothing the gas rather than by generating stronger outflows. We conclude that although higher resolution simulations, and potentially also different supernova implementations, are needed for confirmation, our findings suggest that radiation feedback is more gentle and less effective than is often assumed in subgrid prescriptions.

**Key words:** radiative transfer – methods: numerical – galaxies: evolution.

## 1 INTRODUCTION

To first order, gravity describes the formation of structure in the Universe (Peebles & Yu 1970; Zel'dovich 1970). The formation of galaxies in dark matter (DM) haloes also requires radiative cooling to relieve pressure and dissipate angular momentum (Binney 1977; Rees & Ostriker 1977; Silk 1977). It is also well established that in order to halt the collapse of gas into galaxies, dense substructures, and eventually stars, counteracting feedback processes are required (e.g. White & Rees 1978). Without feedback, galaxies collapse and form stars too efficiently, compared to observations.

Early simulations focused on feedback in the form of supernovae (SNe; e.g. Katz 1992; Navarro & White 1993) and later active galactic nuclei (AGN; e.g. Di Matteo, Springel & Hernquist 2005; Booth & Schaye 2009; Dubois et al. 2010), where the latter is thought to be dominant in massive ('$L > L_*$') galaxies (Bower et al. 2006). However, simulations that include those feedback processes still struggle to produce galaxies that match observations in terms of their star formation histories and morphology (Scannapieco et al. 2012).

Analytical work by e.g. Thompson, Quataert & Murray (2005), Murray, Quataert & Thompson (2005, 2010), and Murray, Ménard & Thompson (2011) suggests that radiation feedback may be an important missing ingredient. Recent hydrodynamical (HD) simulations therefore often enlist stellar radiation in their subgrid feedback models (e.g. Brook et al. 2012; Agertz et al. 2013; Stinson et al. 2013; Agertz & Kravtsov 2015; Ceverino et al. 2014; Hopkins et al. 2014; Kannan et al. 2014a,b; Roškar et al. 2014). The added radiation feedback usually contributes directly to direct suppression of star formation, and increases galactic outflows, which can expel the gas altogether and enrich the intergalactic medium with metals. The idea of radiation feedback has proven so successful that most cosmological simulations nowadays invoke it in some form, although the implementations vary a lot, and they are often motivated empirically rather than physically. Radiation feedback on galactic scales is usually modelled with subgrid recipes in otherwise purely HD codes. These HD recipes must make a number of assumptions about e.g. the absorption of photons, mean free paths, and shielding. They can thus only to a limited degree be used to investigate how

⋆ E-mail: jokirosdahl@gmail.com

important radiation is for the formation and evolution of galaxies, and how the radiation interacts with the baryons, i.e. how radiation feedback actually works.

The recent literature on simulations of galaxy evolution usually considers three radiation feedback processes: photoionization heating of gas, direct pressure from ionizing photons, and indirect pressure from reprocessed, multiscattering, infrared (IR) photons. Simulations often contain only a subset of these processes, and there is no general consensus on the importance of radiation feedback as a whole, or on which of these processes dominate under which circumstances (see Section 4.4).

A more assumption-free and physically correct description of radiation feedback requires the use of radiation-hydrodynamics (RHD), which models the emission and propagation of photons and their interaction with the gas self-consistently. RHD can help tell us if and how radiation feedback works, and this information can then be used to improve HD subgrid recipes of radiation feedback.

However, RHD is both complex and costly compared to HD. For the most part, it has therefore not been used directly in simulations of structure formation, or more generally in studies of galaxy evolution. In recent years however, the use of RHD has been on the rise in computational astronomy, and RHD implementations have evolved towards being usable in cosmological and galaxy-scale simulations that resolve the interstellar medium (ISM; Wise et al. 2012a,b; Pawlik, Milosavljević & Bromm 2013; Wise et al. 2014).

In Rosdahl et al. (2013, hereafter R13), we presented an RHD implementation in the cosmological code RAMSES (Teyssier 2002), which we called RAMSES-RT. In that paper, we modelled the emission and propagation of photons and their interaction with hydrogen and helium via ionization and heating. In Rosdahl & Teyssier (2015, hereafter R14), we added two aforementioned processes to the implementation, which are thought to be relevant for galactic feedback: radiation pressure, i.e. momentum transfer from photons to gas, and the diffusion and trapping of multiscattered IR radiation in optically thick gas.

In this paper, we use the RHD implementation that we have detailed in the two previous papers to study the effect of stellar radiation feedback on galactic scales. We use a set of RAMSES-RT simulations of isolated galactic disc simulations, where we include stellar radiation feedback, combined with 'thermal dump' SN feedback. The main questions we attempt to answer are as follows:

(i) What role does stellar radiation feedback play in regulating galaxy evolution, and how does this role vary with the mass and metallicity of the galaxy?

(ii) How does the interplay of radiation and SN feedback work? Specifically, does radiation boost the effect of SNe?

(iii) Where stellar radiation feedback plays a role, what is the dominant physical process: photoionization heating, direct pressure from the ionizing photons on the gas or indirect pressure via dust particles UV and reprocessed IR radiation?

In this paper, we study the effects of turning on the stellar radiation in galaxies, while making minimal assumptions about what happens on unresolved scales. While using RHD implies radiation feedback is modelled from 'first principles', we stress that it is still necessary to make a number of approximations, both in the modelling of the radiation itself and in its interaction with gas and dust. Also, and importantly, although we resolve the ISM to some extent, we do not resolve molecular clouds, the scales at which the radiation feedback originates, and at which the radiation couples most efficiently with the gas. We expect the current simulations to give us hints as to what radiation feedback does in reality, and, equally importantly, to teach

us what improvements in modelling and resolution are required in future work.

The structure of the paper is as follows. In Section 2, we present an overview of the code, the setup of galaxy discs of three masses, and details of the modelling of gas, stellar populations, and feedback. In Section 3, we present the results, where we successively incorporate SN and radiation feedback processes and compare their effects on the galaxies. We focus on the suppression of star formation and the generation of outflows, study *how* radiation feedback plays a role, and examine trends with galaxy mass and metallicity. In Section 4, we discuss and justify our main findings on analytic grounds, demonstrate how they are limited by resolution, probe what effects we can expect when the resolution is increased beyond the current limits, and qualitatively compare our results to previous publications. Finally, in Section 5 we summarize our main conclusions and discuss interesting future directions. The appendices provide details on the model we use for stellar population specific luminosities and convergence tests.

## 2 SIMULATIONS

We use RAMSES-RT (R13, R14), an RHD extension of the adaptive mesh refinement (AMR) code RAMSES (Teyssier 2002). RAMSES models the interaction of DM, stellar populations, and baryonic gas, via gravity, hydrodynamics, and radiative cooling. The gas evolution is computed using a second-order Godunov scheme for the Euler equations, while trajectories of collisionless DM and stellar particles are computed using a particle-mesh solver. RAMSES-RT adds the propagation of photons and their on-the-fly interaction with hydrogen and helium via photoionization, heating, and momentum transfer; and with dust particles via heating and momentum transfer. The code solves the advection of photons between grid cells with a first-order moment method and closes the set of radiation transport equations with the M1 relation for the Eddington tensor. The trapped/streaming photon scheme presented in R14 describes the diffusion of multiscattering IR radiation. The radiation in a photon *group*, defined by a frequency interval, is described in each grid cell, by the radiation energy density $E$ (energy per unit volume) and the bulk radiation flux $\boldsymbol{F}$ (energy per unit area per unit time), which corresponds approximately to the radiation intensity integrated over all solid angles. RAMSES-RT solves the non-equilibrium evolution of the ionization fractions of hydrogen and helium, along with photon fluxes and the gas temperature in each grid cell.

Because the timestep length, and therefore the computational load, scales inversely with the speed of light $c$, we apply the so-called reduced speed of light approximation (Gnedin & Abel 2001, R13) in runs that include radiation, to maintain a manageable computing time. In this work, we use a light speed fraction $f_c = 1/200$, i.e. free-streaming photons are propagated at a speed $\tilde{c} = c/200$, such that the timestep is most of the time limited by non-RT conditions, and the slow-down due to RT is only about a factor 2–3 compared to HD simulations, depending on the number of photon groups and processes included (and the inclusion of SN feedback, which limits the timestep as well). We showed in R13 that larger values for $f_c$ than we have chosen here are preferable in simulations of galaxy evolution in order to accurately capture the expansion speed of ionization fronts in the ISM, but the light speed convergence tests presented in Appendix D indicate that our results are robust with respect to the chosen light speed.

We run simulations of isolated rotating disc galaxies of baryonic mass $3.5 \times (10^8, 10^9, 10^{10})\,\mathrm{M}_\odot$ consisting of gas and stars embedded in DM haloes of masses $10^{10}$, $10^{11}$, and $10^{12}\,\mathrm{M}_\odot$, respectively.

**Table 1.** Simulation parameters for the three disc galaxies. The listed parameters are, from left to right: galaxy acronym used throughout the paper, $v_{circ}$: NFW circular velocity, for the IC generation, $R_{vir}$: halo virial radius (defined as the radius at which the DM density is 200 times the critical density at redshift zero), $L_{box}$: simulation box length, $M_{halo}$: DM halo mass, $M_{disc}$: disc galaxy mass in baryons (stars+gas), $f_{gas}$: disc gas fraction in the ICs, $M_{bulge}$: stellar bulge mass in the ICs, $N_{part}$: Number of DM/stellar particles in the ICs, $m_*$: mass of stellar particles formed during the simulations, $\Delta x_{max}$: coarsest cell resolution, $\Delta x_{min}$: finest cell resolution, $Z_{disc}$: disc metallicity.

| Galaxy acronym | $v_{circ}$ (km s$^{-1}$) | $R_{vir}$ (kpc) | $L_{box}$ (kpc) | $M_{halo}$ (M$_\odot$) | $M_{disc}$ (M$_\odot$) | $f_{gas}$ | $M_{bulge}$ (M$_\odot$) | $N_{part}$ | $m_*$ (M$_\odot$) | $\Delta x_{max}$ (kpc) | $\Delta x_{min}$ (pc) | $Z_{disc}$ (Z$_\odot$) |
|---|---|---|---|---|---|---|---|---|---|---|---|---|
| G8 | 30 | 41 | 150 | $10^{10}$ | $3.5 \times 10^8$ | 0.5 | $3.5 \times 10^7$ | $10^5$ | 600 | 2.3 | 18 | 0.1 |
| G9 | 65 | 89 | 300 | $10^{11}$ | $3.5 \times 10^9$ | 0.5 | $3.5 \times 10^8$ | $10^6$ | 600 | 2.3 | 18 | 0.1 |
| G10 | 140 | 192 | 600 | $10^{12}$ | $3.5 \times 10^{10}$ | 0.3 | $3.5 \times 10^9$ | $10^6$ | $10^4$ | 4.7 | 36 | 1 |

The simulation sets, named G8, G9, and G10, after the order-of-magnitude of the baryonic masses, are presented in Table 1, and the parameters listed in the table are explained in what follows. The baryonic mass of the most massive galaxy (G10) is comparable to that of the present-day Milky Way (MW).

For G8 and G9, the host DM haloes are disproportionally low in mass, compared to results from abundance-matching (Moster, Naab & White 2013) and cosmological simulations that match the observed galaxy mass function (Schaye et al. 2015). These under-massive DM haloes are not a major issue for this work, however. We are primarily interested in comparing the relative effects of different feedback processes on the properties of the galaxy disc, for which the DM profile does not play an important role. To verify that our results are insensitive to the mass of the host halo, we have run counterparts of the least massive galaxy, G8, with the halo mass increased to a more realistic value $M_{halo} = 7 \times 10^{10}$ M$_\odot$ (i.e. an increase by a factor of 7 compared to Table 1), while keeping the same resolution. We confirmed that while the simulations were more expensive due to the increased size of the box and number of DM particles, the results were not affected.

### 2.1 Initial conditions

The initial conditions (ICs) are generated with the MAKEDISK[1] code by Volker Springel (see Springel, Di Matteo & Hernquist 2005; Kim et al. 2014). The DM haloes follow an NFW density profile (Navarro, Frenk & White 1997) with concentration parameter $c = 10$ and spin parameter $\lambda = 0.04$. We model the DM in each halo with $N_{part}$ collisionless particles of identical mass. The initial disc consists of gas cells and $N_{part}$ identical mass stellar particles, both set up with density profiles that are exponential in radius and Gaussian in height above the mid-plane. The galaxies also contain stellar bulges with mass one-tenth of the stellar disc mass, represented by $0.1 N_{part}$ particles. The stellar particles that are present at the beginning of the simulation do not perform any feedback. The initial gas profiles do not enforce exact hydrostatic equilibrium. However, the initial (few million years) stabilization of the galaxy, which manifests itself in contraction of the inner dense gas and expansion of the outer diffuse gas, is minor, as can be inferred from plots of the star formation rate (e.g. Fig. 4). The initial temperature of the gas disc is $T = 10^4$ K, and the disc metallicity, $Z_{disc}$, is set to a constant value, either 0.1 or 1 times solar (see Table 1), with the metal mass fraction in the Sun taken to be $Z_\odot = 0.02$. The circumgalactic medium (CGM) initially consists of a homogeneous hot and diffuse gas, with $n_H = 10^{-6}$ cm$^{-3}$, $T = 10^6$ K and zero metallicity. The

cutoffs for the disc's radial and vertical gas profiles, which mark the transition between the disc and CGM, are chosen to minimize the density contrast between the disc edges and the CGM.

### 2.2 Star formation

Star formation follows a standard Schmidt law. In each cell where the gas density exceeds the chosen star formation threshold

$$n_* = 10 \text{ cm}^{-3}, \tag{1}$$

gas is converted into stars at a rate

$$\dot{\rho}_* = \epsilon_{ff} \rho / t_{ff}, \tag{2}$$

where $\rho$ is the gas density and $\epsilon_{ff} = 0.02$ is the star formation efficiency per free fall time, $t_{ff} = [3\pi/(32\,G\rho)]^{1/2}$, where $G$ is the gravitational constant. Collisionless particles of mass $m_*$, representing stellar populations, are formed stochastically from the gas, with the probability of forming one drawn from a Poissonian distribution (for details, see Rasera & Teyssier 2006). Table 1 lists the stellar particle masses used in the simulations. In addition to the density threshold for star formation, we also do not allow stars to form in gas warmer than $T/\mu = 3000$ K, where $\mu$ is the average particle mass in units of the proton mass. We note, however, that our results are insensitive to increasing or even removing the temperature threshold.

### 2.3 SNe feedback

We model SN feedback with a single injection from each stellar particle into its host cell, 5 Myr after the particle's birth, of mass $m_{ej} = \eta_{SN} \times m_*$, and thermal energy $\epsilon_{SN} = \eta_{SN} \times 10^{51}$ erg $m_*/10$ M$_\odot$. We use $\eta_{SN} = 0.2$, roughly corresponding to a Chabrier (2003) stellar initial mass function (IMF). We neglect the metal yield associated with stellar populations, i.e. the stellar particles inject zero metals into the gas.

At our resolution, the 'thermal dump' SN feedback model that we use is known to suffer from numerical overcooling (e.g. Creasey et al. 2011; Dalla Vecchia & Schaye 2012; Creasey, Theuns & Bower 2013), but we use it here, because it is simple and because it allows us to investigate how far radiation feedback can go to compensate for its low efficiency. The coupling between radiation and SN feedback, which we study in Section 3.1.4, could depend on the choice of SN feedback model. More efficient SN feedback might either be amplified more efficiently by the stellar radiation to suppress star formation and increase outflow rates, or conversely, it might dominate completely over the effects of radiation feedback and render it negligible. These considerations are beyond the scope of this paper, but in future work we will combine radiation feedback

---

[1] Adapted to generate RAMSES-readable format by Romain Teyssier and Damien Chapon.

with more efficient recipes for SN feedback, to find what combination produces best agreement with observations (which is not the point of this paper) and to study how the interplay of the feedback processes is affected.

## 2.4 Gas thermochemistry

We evolve the thermochemistry semi-implicitly with the method presented in R13. The method tracks the non-equilibrium cooling rates of hydrogen and helium, here assuming zero incoming photon flux. The ionization fractions of hydrogen and helium are stored in each cell as three passive scalars, which are advected with the gas. We assume hydrogen and helium mass fractions $X = 0.76$ and $Y = 0.24$, respectively, and solar ratios for the metal species, i.e. we track a single scalar representing the metal mass fraction in each cell.

We add the contribution from metals to the cooling rate using tables generated with CLOUDY (Ferland et al. 1998), assuming photoionization equilibrium with the redshift zero Haardt & Madau (1996) UV background. With metal cooling, the gas can in principle cool non-adiabatically to $\sim 10$ K. We do not model the change in the metal cooling rate with the local radiation flux, which may affect galaxy evolution (e.g. Cantalupo 2010; Kannan et al. 2014a). In future work, we will consider more realistic metal cooling, which takes the local radiation flux into account.

## 2.5 Adaptive refinement

In the adaptive refinement scheme of RAMSES, cells can be split into eight child cells of width half that of the parent. The width of a cell is determined by its refinement hierarchy level $\ell$, by $\Delta x_\ell = L_{box}/2^\ell$, where $L_{box}$ is the simulation box width. The maximum and minimum cell widths, $\Delta x_{max}$ and $\Delta x_{min}$, are determined by the enforced minimum and maximum allowed refinement levels in a simulation, which in this work are $\Delta x_{max} = 2\text{--}5$ kpc and $\Delta x_{min} = 18\text{--}36$ pc, depending on the simulation set (see Table 1). Adaptive refinement follows mass: a cell is refined if it contains eight or more collisionless particles, if the cell gas mass $m_{cell} > 12\, m_*$, or if $\Delta x$ is more than a quarter of the local Jeans length.

## 2.6 Artificial 'Jeans pressure'

We impose a pressure floor on gas to prevent artificial fragmentation below the Jeans scale (Truelove et al. 1997). The Jeans length-scale for a self-gravitating cloud is

$$\lambda_J = \sqrt{\frac{\pi c_s}{G \rho}} = 16 \text{ pc} \left(\frac{T}{1 \text{ K}}\right)^{1/2} \left(\frac{n_H}{1 \text{ cm}^{-3}}\right)^{-1/2}, \quad (3)$$

where $c_s = \sqrt{\gamma k_B T / m_p}$ is the sound speed, and we assumed a ratio of specific heats of $\gamma = 1.4$, appropriate for a monatomic gas. From equation (3), the requirement that the Jeans length is resolved by at least $N$ cell widths becomes a temperature floor of the form

$$\frac{T}{1 \text{ K}} \geq \frac{n_H}{1 \text{ cm}^{-3}} \left(\frac{N \Delta x}{16 \text{ pc}}\right)^2. \quad (4)$$

We apply this floor in the form of an effective temperature function

$$T_J = T_0\, n_H / n_*, \quad (5)$$

where we use $T_0 = 500$ K in all our simulations, ensuring that the Jeans length is resolved by a minimum number of six cell widths in G8 and G9 and three cell widths in G10. The pressure floor is

non-thermal, and added to the physical temperature, $T$, and hence we can have $T \ll T_J$.

## 2.7 Radiation feedback

We include the emission and propagation of stellar radiation, and its interaction with the gas. The mass-, age-, and metallicity-dependent stellar specific luminosities are extracted on the fly from the spectral energy distribution (SED) model of Bruzual & Charlot (2003), as described in R13, assuming a Chabrier (2003) IMF. Stellar particles inject photons into their host grid cells at every fine RHD timestep.

We bin the radiation into five photon groups, defined by the photon energy intervals listed in Table 2. The groups are, in order of increasing energy, IR, optical, and three groups of ionizing ultraviolet (UV) photons, bracketed by the ionization energies for H I, He I, and He II. We include the first two groups only in runs with radiation-dust interactions, while we include the three UV groups in all runs with radiation. Appendix A describes how the stellar luminosities, photon group energies, and ionization cross-sections are derived from the SED model. Table 2 lists typical values for the energies and cross-sections, along with their variations over the simulation run-time.

An important advantage of the moment method that we use for the radiative transfer (RT) is that the computational cost, i.e. the runtime of the simulations, is *independent* of the number of radiation sources. With the alternative class of ray-tracing methods (e.g. Wise & Abel 2011), the computational cost increases more or less linearly with the number of sources, which requires remedies to keep down the computing cost, such as merging of sources or rays (e.g. Pawlik & Schaye 2008) and/or turning them off after a few Myrs. Turning them off seems acceptable, considering that the luminosity of a stellar population has dimmed by orders of magnitude 10 Myr after its birth (see Fig. A1). However, Kannan et al. (2014a) have pointed out that the cumulative radiation from many such dim old sources may play a role in stellar feedback. Since we do not have an issue with the number of radiation sources in our implementation, stellar particles are never turned off after their birth, and the cumulative radiation from old populations is included.

We implement three 'separate' radiation feedback processes, describing different interactions between the radiation and gas.

(i) Photons ionize and heat the gas they interact with, following the thermochemistry described in R13, typically heating the ionized gas to $\approx 2 \times 10^4$ K. All our runs with radiation include this process. We describe in Appendix A how we use the SED model from Bruzual & Charlot (2003) to derive photoionization cross-sections, which are typically a few times $10^{-18}$ cm$^2$ for H I, He I, and He II.

(ii) Direct pressure, i.e. momentum transfer, from the ionizing photons on to the gas.

(iii) Indirect radiation pressure on the gas, via dust particles, from the ionizing photons, optical photons, and from reprocessed IR radiation, where the latter multiscatters.

R14 contains a detailed description of the implementation and tests of the latter two processes, including the diffusion, pressure, and work of multiscattered IR radiation. We perform the correct diffusion of IR radiation by a partition in every cell into free-streaming and trapped photons, where the trapped photons dominate in the case of large optical depth on the scale of the cell width.

We will refer to the various radiation feedback processes under the collective acronym of RT feedback. RT feedback may thus refer to the inclusion of any or all of the radiation feedback processes under consideration. We will successively add the three RT processes

**Table 2.** Photon group energy (frequency) intervals and properties. The energy intervals defined by the groups are indicated in units of eV by $\epsilon_0$ and $\epsilon_1$ (in units of Å by $\lambda_0$ and $\lambda_1$). The next four columns show photon properties derived every five coarse time-steps from the stellar luminosity-weighted SED model (see Fig. A1 and surrounding text). These properties evolve over time as the stellar populations age, and the approximate variation is indicated in the column headers. $\bar{\epsilon}$ denote the photon energies, while $\sigma_{\mathrm{H\,I}}$, $\sigma_{\mathrm{He\,I}}$, and $\sigma_{\mathrm{He\,II}}$ denote the cross-sections for ionization of hydrogen and helium, respectively. $\tilde{\kappa}$ is the dust opacity. The gas opacity scales with the gas metallicity, $\kappa_i = \tilde{\kappa}_i\, Z/Z_\odot$, where $i$ denotes the photon group.

| Photon group | $\epsilon_0$ (eV) | $\epsilon_1$ (eV) | $\lambda_0$ (Å) | $\lambda_1$ (Å) | $\bar{\epsilon}$ (eV) $\pm 10$ per cent | $\sigma_{\mathrm{H\,I}}$ (cm$^2$) $\pm 5$ per cent | $\sigma_{\mathrm{He\,I}}$ (cm$^2$) $\pm 5$ per cent | $\sigma_{\mathrm{He\,II}}$ (cm$^2$) $\pm 5$ per cent | $\tilde{\kappa}$ (cm$^2$ g$^{-1}$) |
|---|---|---|---|---|---|---|---|---|---|
| IR | 0.10 | 1.00 | $1.2 \times 10^5$ | $1.2 \times 10^4$ | 0.6 | 0 | 0 | 0 | 10 |
| Opt | 1.00 | 13.60 | $1.2 \times 10^4$ | $9.1 \times 10^2$ | 5.5 | 0 | 0 | 0 | $10^3$ |
| UV$_{\mathrm{H\,I}}$ | 13.60 | 24.59 | $9.1 \times 10^2$ | $5.0 \times 10^2$ | 18.0 | $3.3 \times 10^{-18}$ | 0 | 0 | $10^3$ |
| UV$_{\mathrm{He\,I}}$ | 24.59 | 54.42 | $5.0 \times 10^2$ | $2.3 \times 10^2$ | 33.4 | $6.3 \times 10^{-19}$ | $4.8 \times 10^{-18}$ | 0 | $10^3$ |
| UV$_{\mathrm{He\,II}}$ | 54.42 | $\infty$ | $2.3 \times 10^2$ | 0 | 60.0 | $9.9 \times 10^{-20}$ | $1.4 \times 10^{-18}$ | $1.3 \times 10^{-18}$ | $10^3$ |

to our simulations, to probe their respective importance. Always included in RT feedback is photoionization and photoionization heating, from the three UV photon groups. On to that we add direct pressure from photoionization (again only the three UV groups). Finally, we add radiation–dust interactions, from all five groups.

Each photon group $i$ has a dust-interaction opacity, $\tilde{\kappa}_i$, listed in the rightmost column of Table 2. The gas absorbs momentum from the photons (via dust) with the gas opacity

$$\kappa_i = \tilde{\kappa}_i\, Z/Z_\odot, \tag{6}$$

i.e. in our model, the dust content simply scales with the metallicity of the gas. Higher energy photons (all but IR) absorbed by dust are reprocessed, i.e. re-emitted, into the IR group, while IR photons are (multi-) scattered by the dust.

For the IR, we assume an opacity of $\kappa_{\mathrm{IR}} = 10\, Z/Z_\odot\ \mathrm{cm^2\,g^{-1}}$, while for the higher energy photons we assume $\kappa_{\mathrm{UV}} = 10^3\, Z/Z_\odot\ \mathrm{cm^2\,g^{-1}}$, i.e. a hundred times higher than that of the IR. These opacities are physically motivated from a combination of observations and dust formation theory of the ISM and stellar nurseries (Semenov et al. 2003 for IR, Li & Draine 2001 for higher energy radiation), but they are uncertain by a factor of few, due to model uncertainties and the temperature dependence, which we ignore. Similar values have been used in e.g. Hopkins, Quataert & Murray (2012a), Agertz et al. (2013), and Roškar et al. (2014). The IR opacity we use is at the high-end of what is usually considered in the literature, which is $\tilde{\kappa}_{\mathrm{IR}} \approx 5$–$10\ \mathrm{cm^2\,g^{-1}}$. We have tested and confirmed that our results are insensitive to order-of-magnitude variations in the dust opacities (see Section 4.3).

There are two important exceptions from the default behaviour of the implementation described in R14.

First, our resolution of $\sim 10$ pc does not allow us to accurately capture the regime where dust is optically thick to photons, and radiation and dust are coupled via absorption and blackbody emission. For this reason, and also for the sake of simplicity, we exclude the dust temperature evolution (section 2.3.2 in R14), where the gas temperature is coupled directly to the IR radiation temperature via the Planck cross-section. We decouple the dust temperature by simply setting the Planck cross-section to zero (while keeping a non-zero Rosseland opacity).

The second change is that we assume a fully directional radiation in each cell for the free-streaming radiation pressure (R14, equation 28), by using a renormalized radiation flux magnitude of $\tilde{c}E$, rather than the actual radiation flux of $|\mathbf{F}| \leq \tilde{c}E$. We do this to counter a resolution effect, as the reduced flux, $f_\gamma \equiv |\mathbf{F}|/\tilde{c}E \leq 1$, takes a few ($\sim 5$) cell widths to evolve to unity with our advection

scheme, even with free-streaming radiation. We demonstrate this numerical effect with a simple idealized experiment in Appendix B. For the cell containing the emitting source, this resolution artefact is obvious, since the radiation is isotropic and hence has zero bulk flux (only $E$ is incremented with stellar emission). The lack of bulk radiation flux very close to the emitting stellar particles diminishes the effect of radiation pressure, especially since it turns out that H II regions are often poorly resolved in our simulations. Therefore, we apply this *full reduced flux approximation* ($f_\gamma = 1$) for the radiation pressure, to compensate for resolution effects. It can then be argued that we overestimate radiation pressure, especially in regions where cancellation effects are relevant, but since it turns out that radiation pressure is very weak in our simulations, we prefer to be in danger of overestimating rather than the opposite. We do not apply the full reduced flux approximation for the IR photon group, since pressure from the IR radiation, in the limit where the optical depth is not resolved, is accurately captured by the radiation trapping scheme (R14).

Fig. 1 illustrates the distribution of photons, for the five radiation groups, in one of our runs of the intermediate mass galaxy disc (G9). The figure shows mass-weighted averages along lines-of-sight (LOS) of photon fluxes, integrated over all solid angles, i.e. the mapped quantity is $\tilde{c}E$, where $\tilde{c}$ is the reduced speed of light and $E$ is the radiation energy density. From left to right, the maps show photon groups with increasing energy, starting with IR on the far left, the optical, and finally the three ionizing groups. The photon fluxes differ greatly between the photon groups, decreasing with increasing photon energy. We use different colour scales, such that the logarithmic range is the same, but the upper limit roughly matches the maximum flux in each set of face-on/edge-on maps. For the highest energy group (far right), the low luminosity is simply due to the low emissivity from the stellar populations (see Fig. A1, where we plot the emissivity of the stellar populations). For the two lower energy ionizing groups (second and third from right), the stellar emissivity is similar to that of the optical group, yet the galaxy luminosity is clearly much lower than in the optical. This is due to the much more efficient absorption of the ionizing photons. For photoionization of hydrogen and helium, the opacities are $\sigma/m_{\mathrm{p}} \sim 6 \times 10^5\ \mathrm{cm^2\,g^{-1}}$, where $\sigma \sim 10^{-18}\ \mathrm{cm^2}$ is the photoionization cross-section (see Table 2 and Appendix A) and $m_{\mathrm{p}}$ is the proton mass, while for the optical group the opacity is $\kappa_{\mathrm{Opt}} = \tilde{\kappa}_{\mathrm{Opt}} Z/Z_\odot = 10^2\ \mathrm{cm^2\,g^{-1}}$. Hence, the difference in opacities is more than three orders of magnitude. While the ionizing photons are absorbed close to their emitting sources, the optical photons are much more free to propagate through the disc and
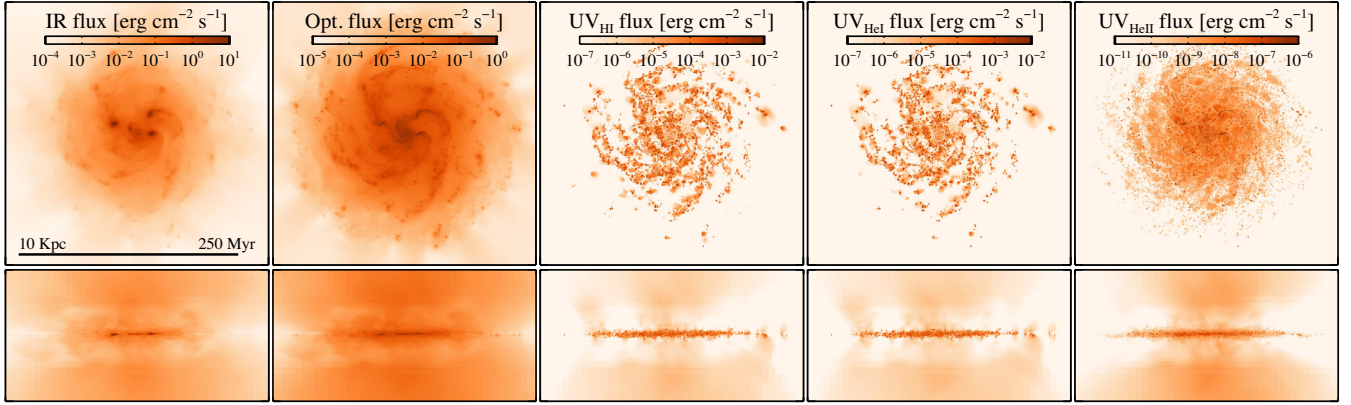
**Figure 1.** Illustration of radiation flux in the five photon groups included in this work. The maps show density-weighted solid-angle integrated photon fluxes, $\tilde{c}E$, along the LOS in the G9 galaxy with SN and full RT feedback (G9_SN_RHPD) at 250 Myr. The photon groups are shown by increasing photon energy, from left to right. The upper row shows the galaxy face-on and the lower row shows it edge on. The much larger contrast in the fluxes of the ionizing photons (three rightmost panels), owes to their much shorter mean free paths. Also, to a smaller degree, the optical photons have larger contrast than IR radiation, for the same reason. For the corresponding distribution of stars and gas in the same snapshots, this figure can be compared to Fig. 3 (bottom-left panel).
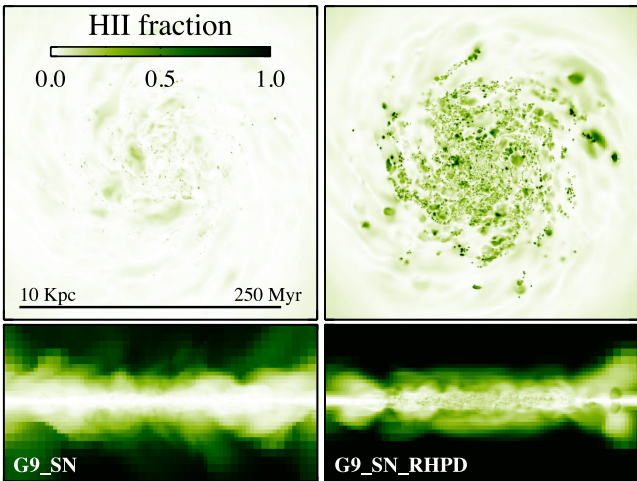


**Figure 2.** Ionized hydrogen fractions in the G9 galaxy at 250 Myr. The maps show mass-weighted ionized fractions along the LOS, for SN feedback only (left, G9_SN) and added (full) radiation feedback (right, G9_SN_RHPD). The right map is the same snapshot as shown in the panels of Fig. 1.

escape from it. The direct stellar IR emission is relatively dim, about three orders of magnitude lower than that of the optical group, yet the maps on the far left show that the radiation energy flux is highest in the IR group. This is because the IR photons are mostly reprocessed from the optical and UV photons, which are captured by the dust and re-emitted into the IR.

Fig. 2 illustrates the effect of the radiation on the hydrogen ionization fractions in the gas, which are tracked by the code. The left-hand panel shows a run with SN feedback only, while the right-hand panel shows the same galaxy also with full RT feedback, which results in an abundance of dense photoionization-powered H II regions.

## 2.8 Overview

Table 1 lists the properties of the simulated galaxies. We run each simulation for 500 Myr. Table 3 lists the six combinations of four feedback processes included in the simulations: no feedback at all (NOFB), SN feedback only (SN), with added radiation feedback with

**Table 3.** Feedback processes included in the simulations.

| Feedback acronym | SN feedback | Radiation heating | Direct rad. pressure | Dust pressure |
|---|---|---|---|---|
| NOFB | | | | |
| SN | ✓ | | | |
| SN_RH | ✓ | ✓ | | |
| SN_RHP | ✓ | ✓ | ✓ | |
| SN_RHPD | ✓ | ✓ | ✓ | ✓ |
| RHPD | | ✓ | ✓ | ✓ |

radiation heating only (SN_RH), with added direct pressure from ionizing photons (SN_RHP), with added radiation pressure on dust, and optical and (reprocessed) IR radiation groups (SN_RHPD), and, finally, with all radiation feedback processes included, but without SN feedback (RHPD). The name of each run is a combination of the acronyms from Tables 1 and 3, e.g. the name G9_SN_RHP represents the G9 galaxy (baryonic mass of $3.5 \times 10^9$ M$_\odot$), simulated with SN feedback and ionizing stellar radiation with heating and direct pressure.
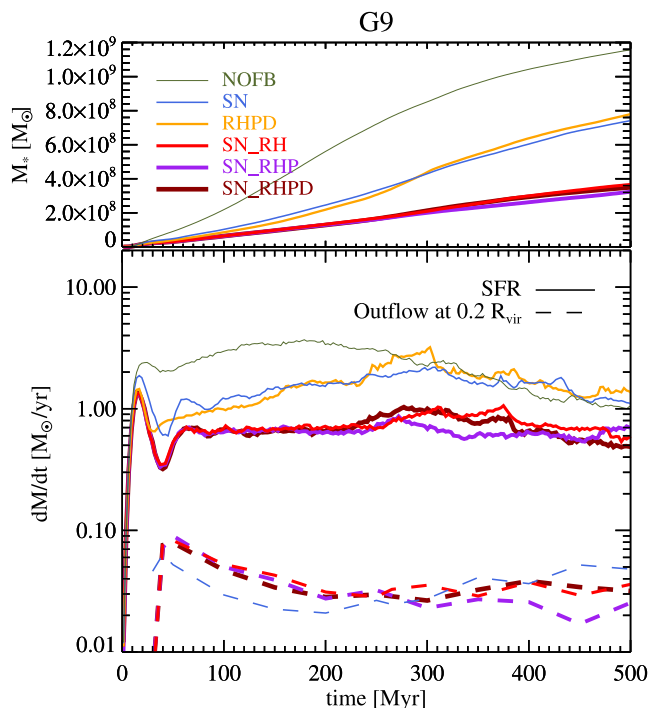
## 3 RESULTS

We now turn to the simulated galaxy discs and examine the impact of radiation feedback and the interplay of radiation and SN feedback. We start with the intermediate-mass galaxy, which has the highest resolution in terms of the number of volume/particle elements, and then consider in turn, with somewhat less detail, the more massive G10 galaxy and the less massive G8 galaxy.

## 3.1 G9: intermediate mass gas-rich galaxy

We first focus on the intermediate mass galaxy, G9 ($\approx$ one-tenth the baryonic mass of the MW), and we begin by considering the qualitative effects of the different feedback processes on the morphology of the disc. Fig. 3 shows maps of stellar density and total hydrogen column density, face on and edge on, at 250 Myr, which is half the run duration. Without feedback (top-left panel), the galaxy contains many cold star-forming clumps interconnected by narrow gas filaments. SN feedback (top-right panel) dramatically reduces star and clump formation, especially at large radii, smooths out the gas
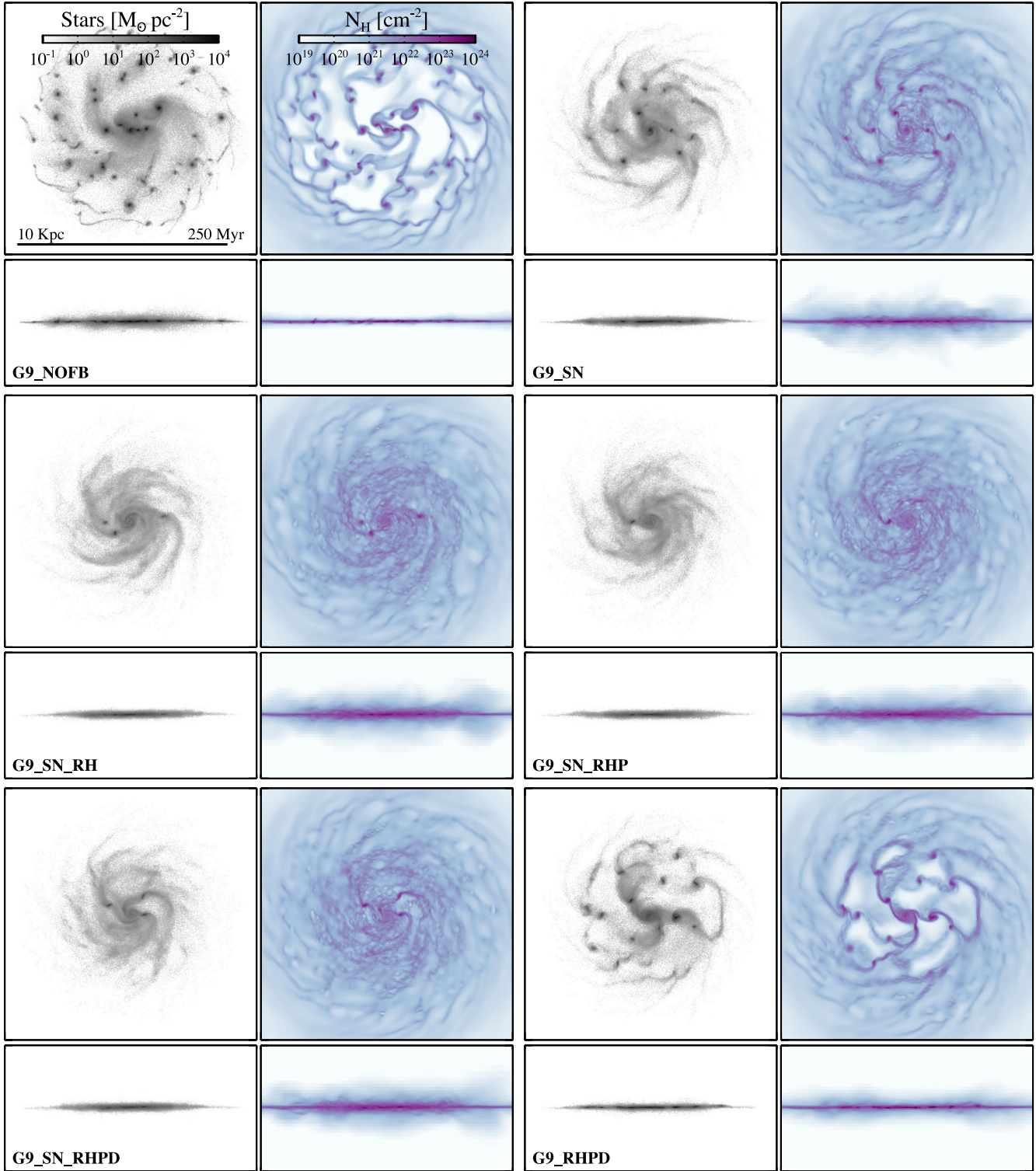
**Figure 3.** Maps of the G9 galaxy (roughly 10 times less massive in baryons than the MW) at 250 Myr, for the different feedback runs. Each panel shows face-on and edge-on views of the stellar density (left) and the hydrogen column density (right). From left to right, top to bottom, the panels show the runs without feedback (NOFB), SN feedback only (SN), SN and radiation heating (SN_RH), SN+radiation heating + direct pressure (SN_RHP), SN + radiation heating + direct + dust pressure (SN_RHPD), and radiation heating + direct + dust pressure (RHPD). The physical length-scale and the colour scales for the stellar and gas column densities are shown in the top left-hand panel. The addition of radiation feedback smooths and thickens the disc, compared to SN feedback only. The respective additions of direct UV radiation pressure and then optical and IR pressure have little effect.

We can probe the importance of radiation pressure by comparing the curves where SN feedback is combined with successive introductions of radiation feedback processes, i.e. photoionization heating, direct ionizing radiation pressure, and radiation pressure on dust. The stellar mass formed is very similar, indicating that radiation heating is the dominant radiation feedback process.

The $\lesssim 10$ per cent variation in the stellar mass formed at the end of the runs for the various radiation feedback processes, is too slight to require serious interpretation. It is likely a random effect where small variations in the feedback model trigger massive clump formation at different times in the simulations. Individual clumps can dominate the star formation for tens of Myrs, while they migrate to the centre of the disc. While these clump formations are likely random, we cannot rule out the possibility that these effects of successively added radiation feedback processes are systematic. If the effect is real and non-stochastic, the way it works is somewhat counter-intuitive, as the addition of radiation pressure on dust and the subionizing photon groups (SN_RHPD) *boosts* star formation. This implies *negative feedback*, which can be explained by a scenario where radiation pressure sweeps the gas into concentrated star-forming shells or clumps. However, we do not see a negative feedback effect from radiation pressure on dust in the other galaxies considered in this paper, and hence we conclude that it is a random effect, rather than systematic.
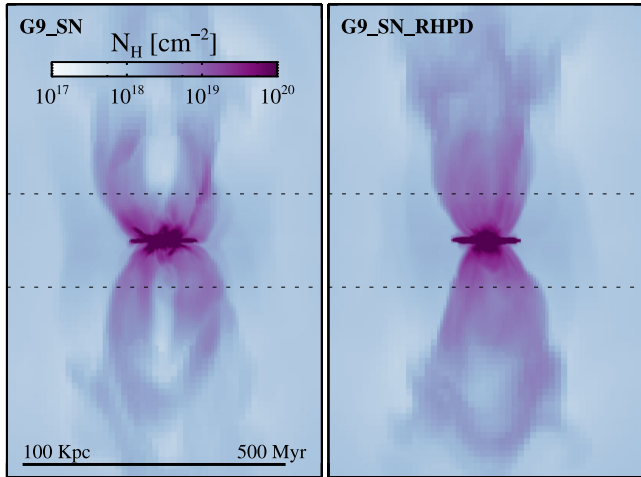
Focusing on the star formation rates for the different feedback processes, in the bottom panel of Fig. 4, we see that the combined SN+RT feedback flattens out the star formation history compared to the case of no feedback or individual SN or RT feedback. The star formation rates decline in the latter half of the runs with no feedback or individual SN or RT feedback. This is due to the galaxy disc starting to be starved of gas. The initial disc gas mass is $\approx 2 \times 10^9 \, \mathrm{M_{\odot}}$, and it is clear from the upper panel that a considerable fraction of this mass has already been converted into stars at 500 Myr. This narrows the difference in star formation rates between the runs: while the rate is suppressed by a factor $\approx 2$ at 500 Myr by the combination of SN and RT feedback, and not suppressed at all by only SN or RT feedback, the suppression factor is much higher before gas depletion sets in, peaking at a factor $\approx 5$ at $\approx 150$ Myr for the combined feedback case and a factor 2–3 for the 'single' feedback case (excluding the first $\approx 50$ Myr, when the disc is relaxing).

### 3.1.2 Outflows

Galaxies produce outflows, and it has been suggested that radiation feedback, and radiation pressure in particular, may be important for generating these galactic winds (Murray et al. 2011). Fig. 5 shows edge-on maps of the total hydrogen column density for the G9 galaxy at 500 Myr, with SN feedback only (left) and with added full RT feedback (right). The panels show that winds are generated in the G9 galaxy. The winds are produced by SN feedback: maps (not shown) with no feedback or RT feedback only show no sign of winds. The figure reveals slightly different wind morphologies, with the SN_RHPD case showing a more collimated wind than the SN run, where the wind seems to form a conical shell, i.e. with a gas-free zone along the z-axis through the centre of the disc. This difference is due to the star formation being more concentrated towards the centre of the disc in the SN+RT feedback case, while it is located in a few clumps at various radii from the centre in the SN case.

We consider the winds more quantitatively in the dashed curves in the lower panel of Fig. 4, which show gas outflow rates across disc-parallel planes at $|z| = 17.8$ kpc, or $0.2 \, R_{\mathrm{vir}}$, in each direction



**Figure 4.** Star formation and outflows in the G9 runs with different feedback processes included, as indicated in the legend: no feedback (NOFB), SN feedback only (SN), RT feedback only with all processes activated (SN_RH), SN+RT feedback with RT heating only (SN_RHP), the same with added direct ionizing radiation pressure (SN_RHPD), and then with added lower energy radiation and dust pressure (RHPD). Upper panel: stellar mass formed over time. Lower panel: star formation rates (solid lines) and outflows across planes at distances of $0.2 \, R_{\mathrm{vir}}$ from the disc plane (dashed lines).

distribution, and thickens the gas disc compared to the no feedback case. The inner $\sim 3$ kpc from the centre of the galaxy remain quite clumpy, however. The addition of ionizing radiation and photoionization heating (middle-left panel) adds to the effect of SN feedback by further smoothing the morphology of the galaxy, and further reducing the number of clumps. The addition of radiation pressure, direct (middle right) and on dust (bottom left), has little impact. With SN feedback excluded, radiation heating and pressure on its own (bottom right) is insufficient to prevent massive clump formation in the galaxy, and it is noticeably more clumpy and thinner than with SN feedback only.

### 3.1.1 Star formation

Star formation is the most direct probe of the efficiency of feedback processes. The more efficient the feedback, the more it will reduce and regulate star formation. Fig. 4 shows, for the G9 galaxy, the cumulative stellar mass formed over time (upper panel) and star formation rates (solid lines in the lower panel). These results are in line with the qualitative effects we saw in the previous maps. Compared to the no feedback case, turning on SN feedback reduces the formation of stars by about 35 per cent at 500 Myr. Turning instead to radiation feedback, with both the pressure terms included, gives a very similar reduction in the star formation. Combining SN and full radiation feedback (three thickest curves) considerably reduces the star formation again, by $\approx 70$ per cent compared to the no feedback case, and by $\approx 50$ per cent compared to the cases with SN or radiation feedback only.

**Figure 5.** Outflows from the G9 galaxy at 500 Myr. The maps show total hydrogen surface density for SN feedback only (left) and added (full) radiation feedback (right). The time, colour-, and length-scales are marked in the left map. Dotted horizontal lines mark planes $0.2\,R_{\rm vir}$ from the galaxy plane, where we measure the outflow/inflow rates plotted in Fig. 4.
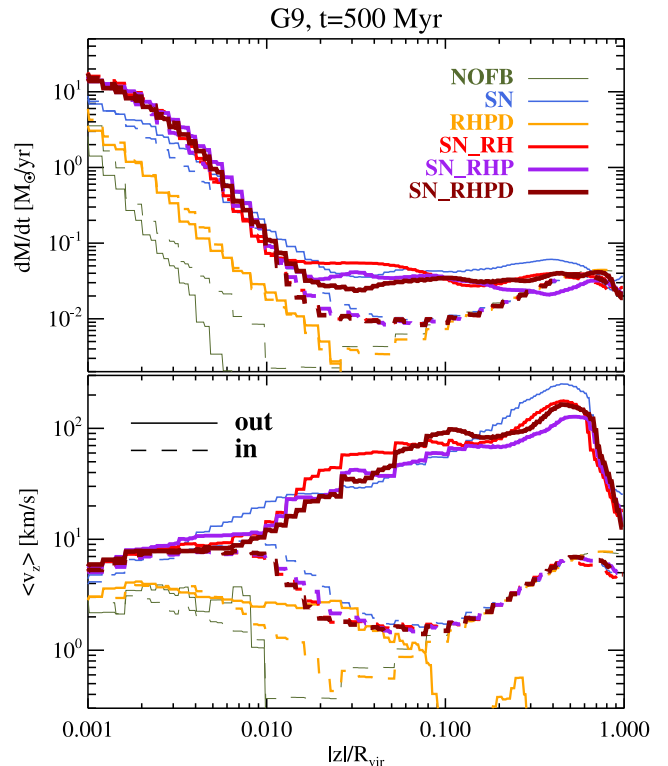


**Figure 6.** Outflow/inflow rates (upper plot) and speeds (lower plot) in the G9 galaxy at 500 Myr.

from the disc. The planes are indicated by dashed horizontal lines in Fig. 5. These are gross outflow rates, i.e. we exclude from the calculation those cells intersecting the planes that have inflowing gas velocity. Where outflows exist across those planes, which is in all the runs with SN feedback included, the outflow rates are similar, within roughly a factor of 2 of each other. RT feedback has very little effect on the outflow rates, regardless of whether or not radiation pressure is included.

Outflows are often quantified in terms of the mass loading factor, which is the ratio between the outflow rate and the star formation rate. In the case of Fig. 4, the mass loading is quite low, i.e. the outflow rates are more than an order of magnitude less than the star formation rates. Although the outflow rates change little with the addition of radiation feedback, the mass loading is typically a few tens of per cent higher, since the star formation is less efficient.

In Fig. 6, we focus on the end-time of 500 Myr and show gas flow rates and mean speeds across parallel planes as a function of distance $|z|$ from the galaxy plane. Here, we split the gas cells into those with outflowing and inflowing $z$-velocities, shown in solid and dashed curves, respectively. RT feedback has very little effect on outflow/inflow rates or speeds when added to SN feedback, except at $|z| \lesssim 3 \times 10^{-3}\,R_{\rm vir} \approx 300$ pc, which is more or less inside the gas disc. At these small distances from the central plane of the disc, RT feedback slightly increases the outflow rates, but notably also the inflow rates, which follow the outflow rates closely. This shows that the RT feedback has the main effect of stirring up the disc gas without ejecting it from the galaxy. This matches with the qualitative differences in the edge-on maps in Fig. 3, where the SN+RT feedback runs can be seen to have a slightly thicker and more diffuse disc than the SN only case. By itself, radiation feedback does not produce outflows (yellow curves in Fig. 6), but it thickens the disc considerably compared to the no feedback case (green curves).

### 3.1.3 The effect of the radiation

We found in the previous subsection that radiation feedback helps regulate star formation in the G9 galaxy. Photoionization heating

dominates the radiation feedback, while radiation pressure appears to have very little effect, if any.

We now consider how the photons affect the properties of the galactic gas. We compare in Fig. 7 temperature–density phase diagrams of gas in the G9 galaxy, for the cases of no feedback (top left), SN feedback only (top right), RT feedback only (bottom left), and combined SN+RT feedback (bottom right). For the RT feedback we have included all radiation feedback processes, but we note that removing radiation pressure, direct or on dust, has no discernible impact on the diagrams.

The diagrams show stacked results from outputs every 50 Myr for $t = 100$–500 Myr,[2] starting after the initial relaxation of star formation seen in Fig. 4. We stack the results to show a crude time-average and reduce the stochastic influence of the formation and destruction of dense clouds, which can shift the maximum densities considerably. Apart from this shift in the maximum density tail, there is no qualitative change in the diagrams between the stacked snapshots. We will refer to results stacked by the same snapshots as 'time-stacked' in the remainder of this paper.

We overplot the star formation thresholds in density and temperature (vertical and horizontal dotted lines), the median temperature per density bin (solid blue curve), and the mass-weighted mean density (solid blue vertical line). We bracket the mean densities by the maximum and minimum means per stacked snapshot (dashed blue vertical lines), indicating the shift caused by the formation and destruction of dense clouds. The diagonal dashed lines indicate the non-thermal Jeans pressure, equation (5), used to prevent resolution-induced fragmentation of gas (Truelove et al. 1997). The artificial pressure term dominates the pressure of gas below this line, i.e. in

---

[2] i.e. from outputs at $t = 100, 150, 200, 250, 300, 350, 400, 450, 500$ Myr.
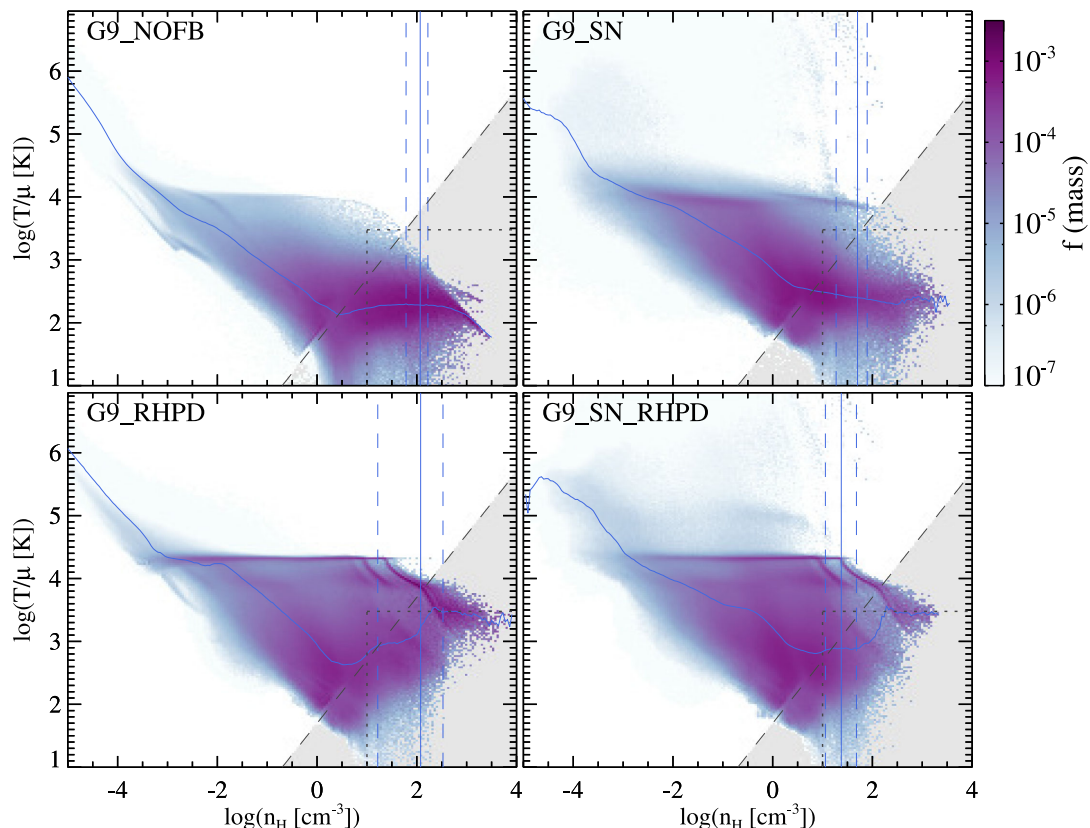
**Figure 7.** Temperature–density phase diagrams, time-stacked from snapshots every 50 Myr after relaxation, in the G9 runs with different feedback processes, as indicated in the top-right corner of each plot. The vertical solid lines show the mass-weighted mean density in each snapshot and the solid curves show the median temperature in each density bin. The dotted lines show the temperature threshold (horizontal) and density threshold (vertical) for star formation. The diagonal dashed lines indicate the non-thermal Jeans pressure, equation (5), which is added to the other pressure terms (thermal pressure and trapped radiation pressure) in the hydrodynamics to prevent artificial fragmentation. Assuming a negligible contribution from trapped IR radiation, the pressure of gas below this line, as indicated by the shaded background colour, is dominated by the artificial Jeans pressure, since the Jeans temperature is larger than $T/\mu$.

the shaded region, making it the de-facto dominant 'feedback' in this high-density low-temperature gas. Without feedback (top left), the Jeans pressure predominantly supports this gas, while adding SN feedback (top right), RT feedback (bottom left), or a combination of the two (bottom right), typically increases the temperature and decreases the density, and thus reduces the amount of gas supported by this artificial pressure. One should keep in mind throughout that the effect of adding SN and RT feedback is somewhat weakened by the existence of this Jeans pressure, which must be in place in all simulations as a last resort to keep gas from collapsing beyond the resolution limits.

In the bottom-left diagram, we see that radiation feedback on its own increases the median temperature of dense gas compared to no feedback (top left), by heating a considerable amount of photoionized gas to $\sim 10^4$ K. However, it has only a tiny impact on the mean density, compared to the no feedback case. Combined with SN feedback, radiation (bottom right) is much more efficient at decreasing the mean density, by almost half a dex compared to SN feedback only.

Judging from the diagrams, the suppression in star formation due to radiation feedback appears to owe to either of two effects, or both (i) direct heating of the gas, which raises it above the temperature threshold of 3000 K for star formation, i.e. gas moves up, or (ii) resistance to gas collapse, indirectly due to the heating, i.e. gas moves to the left. To investigate the direct effect, we have repeated runs G9_RHPD and G9_SN_RHPD, after removing the temperature thresh-

old for star formation. The run with radiation feedback only, i.e. G9_RHPD, shows slight sensitivity to the temperature threshold, with 10 per cent more stellar mass formed at 500 Myr with the threshold removed, while the run with SN+RT feedback (G9_SN_RHPD) actually produces 10 per cent *less* stars if the temperature threshold is removed, which owes to an increase in the SN feedback efficiency. We conclude that the effect of radiation feedback is primarily due to adiabatic resistance to gas collapse, rather than the precise temperature threshold for star formation.

The bottom phase diagrams of Fig. 7 reveal conspicuous features at the right end of the photoionized temperature plateau ($\approx 2 \times 10^4$ K), where the gas temperature decreases and density increases along narrow tracks. They are due to the H II regions being unresolved. The highest temperature tracks consist of single cells filled with radiation at a constant luminosity of a single young stellar particle, and can be accurately reproduced in single cell tests. The lower temperature tracks consist of cells adjacent to those source cells into which the constant luminosity propagates, again at roughly a constant rate. Underresolved H II regions are also visible in Fig. 1, indicated by a high contrast and 'pixellated' peaks for the ionizing photon groups in the three leftmost panels. We will return to this resolution issue in Section 4.1.

Fig. 8 shows the time-stacked mass-weighted density distribution of the gas in the G9 runs. Radiation and SN feedback clearly reduces the maximum gas density, but radiation pressure, when added, has very little effect. The plot supports the previous conclusion that
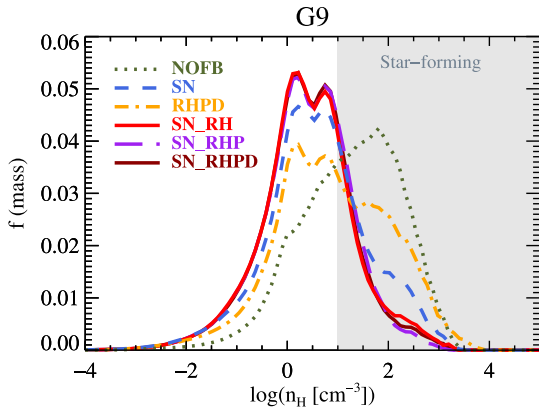
**Figure 8.** Time-stacked mass-weighted density distribution in the G9 galaxy. Star forming gas is indicated by the shaded region. SN and radiation feedback suppresses high gas densities. The suppression from radiation is dominated by radiation heating, but IR and optical pressure on dust provides marginal extra support.

the effect of the radiation heating is to prevent collapse of the gas by increased thermal pressure, which keeps the gas at lower densities. The effect is quite mild though, as the change in the density distribution is small when radiation is added to SN feedback.

### 3.1.4 SN amplification

Radiation can plausibly have the effect of amplifying SN feedback (Pawlik & Schaye 2009; Geen et al. 2015). It can diffuse the surrounding gas, which has the well-known effect of decreasing the cooling rate, which scales with density squared. This in turn can make SNe more effective in stirring up the ISM, suppressing star formation and generating outflows. This may happen as a combination of two effects: by pre-conditioning of the medium by the radiation before the SN events take place, but also in a preventive way, where the radiation feedback shifts the typical star formation densities to lower values, which directly causes SN events to take place at lower densities.

Fig. 9 shows the probability distribution of gas densities at which stellar particles are formed (upper panel) and at which they produce SNe 5 Myr later (lower panel), in the G9 runs with SN only and with full RT feedback added. From the upper panel, we see that the RT feedback shifts star formation to lower densities, which now peak at the star formation threshold, whereas they peak 1.5 dex above the threshold with SN feedback only. One also can read from the cumulative probability curves (solid lines) that with SN feedback only, about 45 per cent of the stars are formed at $n_H \lesssim 10^2$ cm$^{-3}$ (10 times the star formation threshold, $n_*$), while $\approx$70 per cent of the stars form below the same density with RT feedback added. This then translates into a similar difference in the SN densities in the lower plot. With SN feedback only, about 45 per cent of the stars produce SNe in gas with densities below $10 n_*$, while the addition of RT feedback increases this to 70 per cent. This similarity in the characteristic density difference between the two plots indicates that pre-conditioning of the gas by radiation does not play a major role. If it did, we should expect the typical SN densities to shift even further to lower densities.

Even so, we take a closer look at the effect of radiation pre-conditioning in Fig. 10. Here, we plot the probability distribution functions, for SN and SN+RT feedback, for the relative *difference* between surrounding densities at stellar particle birth, $n_{H,b}$, and SN
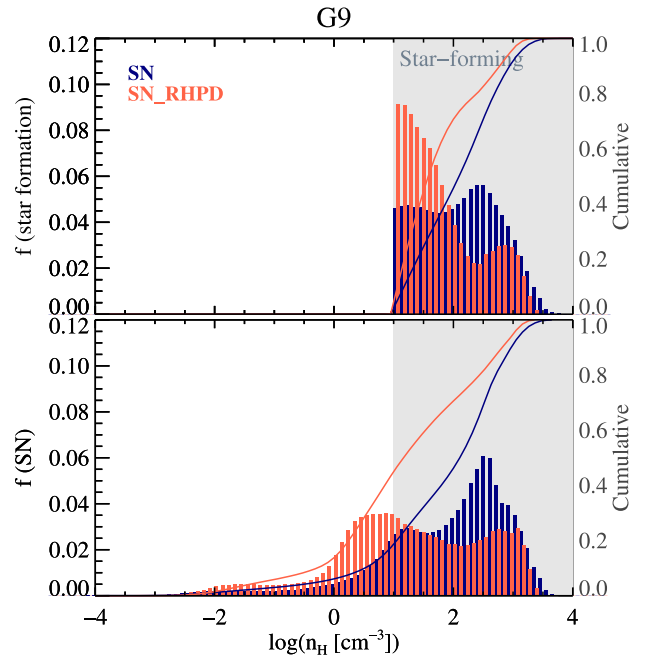


**Figure 9.** Comparison between the SN and SN+RT G9 runs, of the probability distribution functions for the gas density at which stellar particles are created (upper panel) and produce SNe (lower panel). The shaded regions indicate star-forming densities. The solid curves in each panel show the cumulative probabilities. The upper panel indicates that RT feedback lowers the densities at which stellar particles are born, which should increase the SN feedback efficiency by allowing SN events to take place in a lower density medium, as verified in the bottom panel.
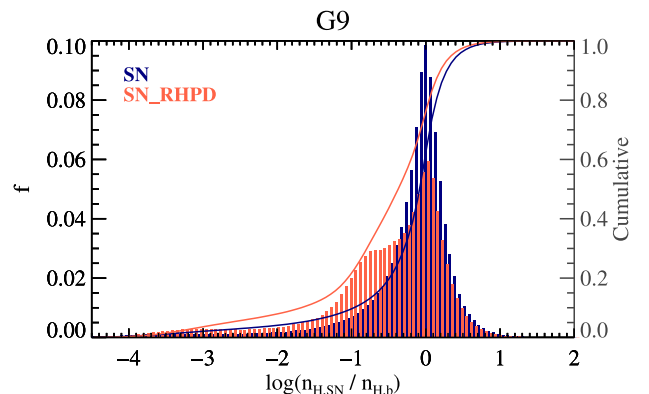


**Figure 10.** Comparison between the G9 runs with SN and SN+RT, of the probability distribution functions for the increase/decrease in the surrounding gas density between stellar particle birth and SN event. A value of zero at the x-axis indicates that the surrounding gas density stays unchanged from birth to SN, while negative/positive values correspond to a decrease/increase in density. The solid curves show the cumulative probabilities. RT feedback has the effect of somewhat, but not dramatically, diffusing the gas around the stellar particles, before they produce SNe.

event, $n_{H,SN}$. The idea is that we remove the effect of the stars being born at lower densities with RT feedback. For the SN feedback only case, we find a strong peak in the probability around $n_{H,SN}/n_{H,b} = 1$, which just means that typically a stellar particle's birth and SN event happen at the same density. A slight majority, $\approx$60 per cent, of the stars produce SNe at lower densities, and there is a tail in the distribution with a few per cent of the SNe exploding at orders of magnitude lower densities. With radiation feedback added, the peak

is still in the same place, but the distribution and the tail is shifted towards lower densities. The effect is not large though.

In addition to giving information about the nature of (possible) SN amplification by radiation feedback, Figs 9 and 10 give us a hint about how radiation feedback suppresses star formation. The radiation shifts star formation to substantially lower densities (Fig. 9), but does not as substantially diffuse gas locally around young stellar particles (Fig. 10), suggesting that the effect of radiation feedback is more to *prevent* the formation of dense clumps, rather than destroying them after they form.

## 3.2 G10: MW mass galaxy

We now turn our attention towards our most massive galaxy, similar in mass to the MW Galaxy. The galaxy is 10 times more massive than the G9 galaxy we have analysed so far, and of interest here is how the galaxy mass affects the radiation feedback. The mass is not the only thing different from the G9 galaxy, however. The metallicity of the gas is 10 times higher and the gas fraction is considerably less: 30 per cent, compared to 50 per cent for the G9 galaxy. It makes sense to change also these properties, since the idea is to roughly follow the stages in the evolution of the present day MW. However, in Section 3.4 we will disentangle the effects of these different galaxy properties on the radiation feedback.

We first consider the qualitative effect of radiation feedback on the galaxy morphology in Fig. 11, where we compare face-on and edge-on maps at 250 Myr. We find no visible effect from radiation pressure, neither direct nor on dust, so we only compare here the case with SN feedback only (G10_SN) and SN + full RT feedback (G10_SN_RHPD). The overall effect of adding RT feedback is less than in the G9 galaxy (Fig. 3), though the disc does become slightly less clumpy and more diffuse compared to SN feedback only. We do not show the no feedback case, but it looks very similar to the case with SN feedback, so also SN feedback is weak in this massive galaxy.

We go on to compare the star formation, in Fig. 12. Here, we again see that all the modelled feedback processes are much weaker than in the previous less massive galaxy. SN feedback initially slightly reduces the star formation compared to the no feedback case, but ends up with *more* stars formed (which is due to the recycling of gas in the SN case, resulting in an effectively larger gas reservoir). In such a massive galaxy, SN feedback is thought to become decreasingly important, and AGN feedback, which is not modelled, may start to dominate (Bower et al. 2006). Also, it is likely that numerical overcooling becomes stronger, due to the increasing gravitational potential, gas densities, metallicity, and decreasing physical resolution (although the larger stellar particle mass should somewhat compensate by injecting more energy per SN event).

In this galaxy, radiation feedback has a stronger effect on the star formation than SNe, though the effect is still weak, with an $\approx 7$ per cent reduction in the stellar mass formed (at 500 Myr) with RT feedback only, and $\approx 10$ per cent if combined with SN feedback. The slightly increased feedback efficiency when combined with SNe hints at an amplification effect, but the effect is small. Radiation heating dominates the radiation feedback, as adding radiation pressure and dust interactions has little effect on the star formation.

Outflows rates across planes $0.2\,R_{\rm vir}$ (38.4 kpc) from the disc are shown by dashed lines in the bottom panel of Fig. 12. Outflows appear to be powered nearly exclusively by SN feedback, since the rates remain virtually unchanged after the addition of radiation
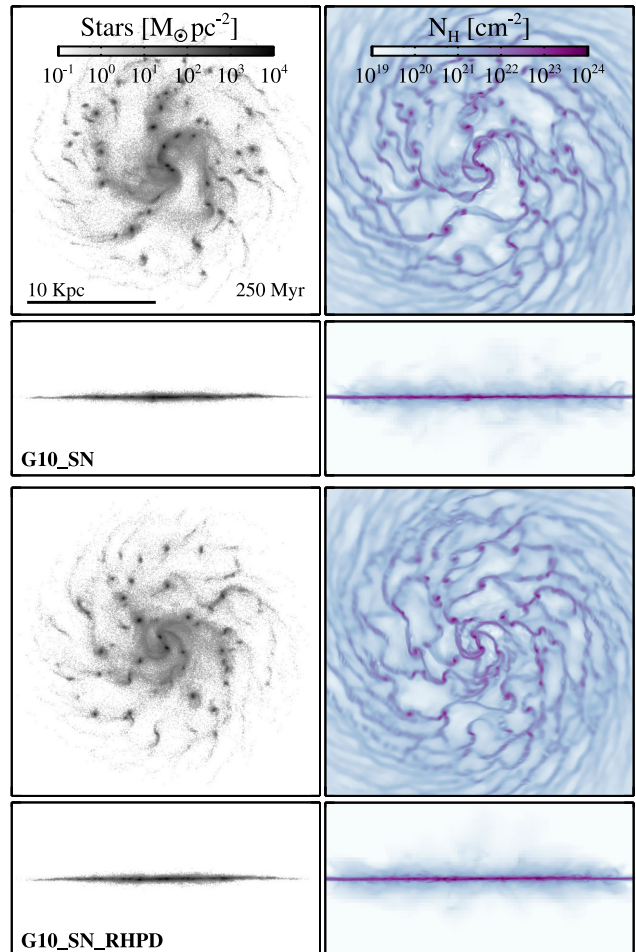


**Figure 11.** Maps of the G10 galaxy (baryonic mass of $3.5 \times 10^{10}\,{\rm M_\odot}$) at 250 Myr, for SN feedback only (upper panel) and full radiation feedback (lower panel). Each panel shows face-on and edge-on views of the stellar density (left) and total hydrogen column density (right). Radiation feedback has little noticeable effect in this galaxy, and in fact the same applies for SN feedback (the comparison to no feedback is not shown).

feedback (of any sort). The mass loading factor of the outflow remains at $\lesssim 0.1$, similar to the G9 galaxy.

## 3.3 G8: gas-rich dwarf

We now consider variations with RT feedback in the least massive galaxy, G8. Its properties only differ from those of the intermediate mass G9 galaxy in terms of the halo and galaxy mass. The gas fraction and metallicity are unchanged, at 50 per cent and $0.1\,{\rm Z_\odot}$, respectively.

We begin with a qualitative comparison of morphologies with the inclusion of different feedback processes, shown in Fig. 13. We compare the cases of no feedback (top panel) full RT feedback (i.e. heating, direct, and dust pressure, middle panel), and SN+RT feedback (bottom panel). RT feedback on its own is clearly much more efficient in this galaxy than in the previous, more massive ones. It completely suppresses the formation of massive clumps, smooths out density contrasts, and considerably reduces the formation of stars. We do not show the case with SN feedback only, but note that in the weak gravitational potential of the G8 galaxy, it has a similar
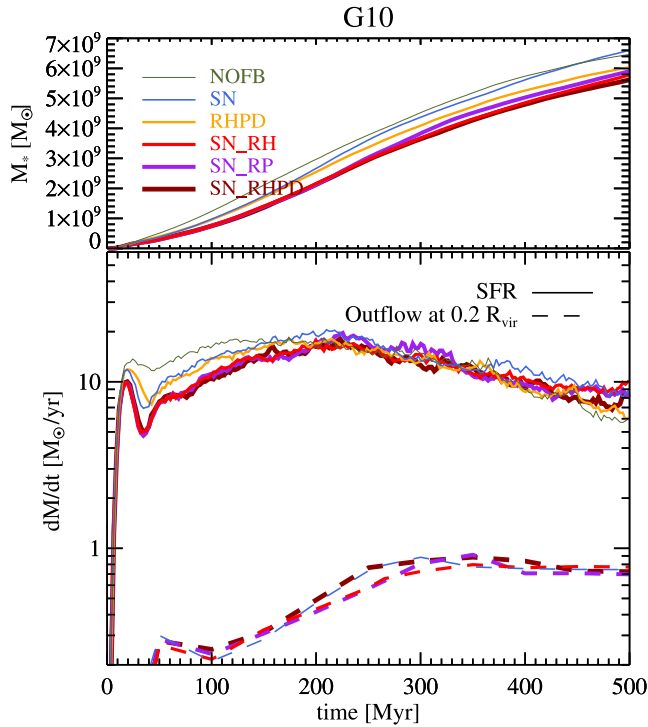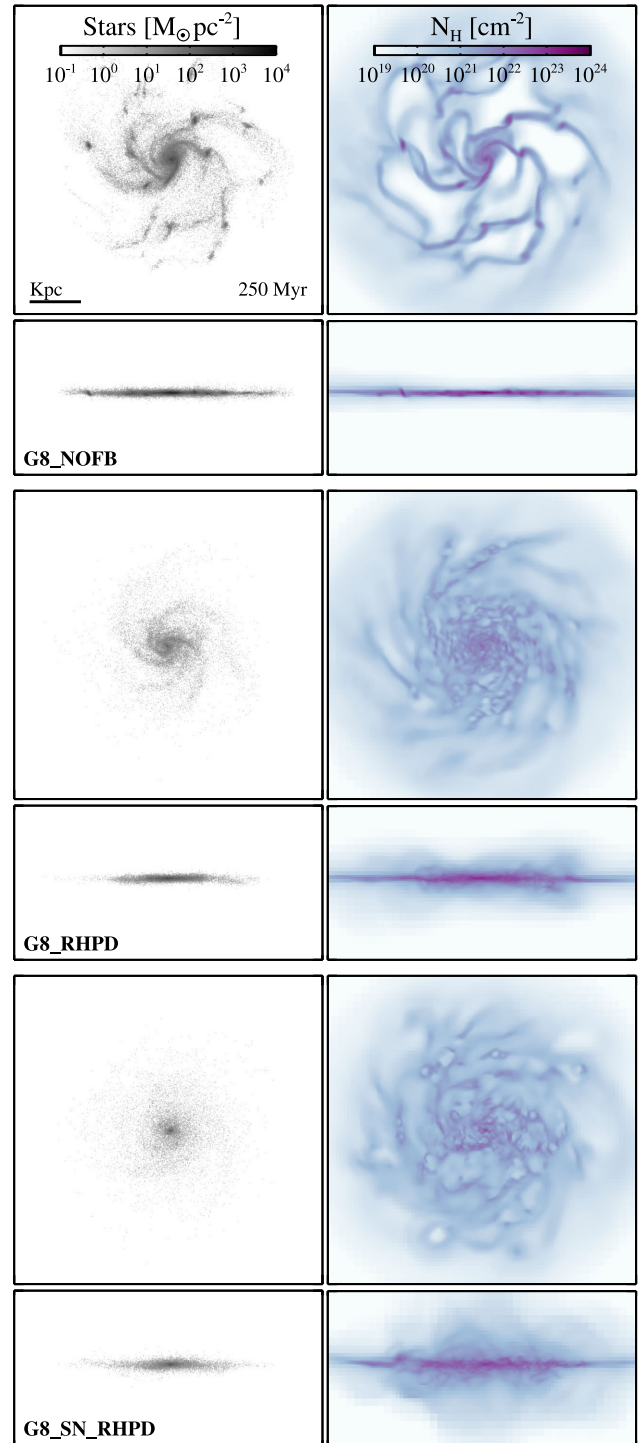
**Figure 12.** Star formation and outflow rates in the G10 runs with different feedback processes included, as indicated in the legend. Upper panel: stellar mass formed over time. Lower panel: star formation rates (solid lines) and outflow rates across planes at distances of $0.2 R_{vir}$ from the disc plane (dashed lines). Feedback is much less effective here than in the less massive G9 galaxy (cf. Fig. 4). Radiation heating suppresses star formation more than SN feedback, but the effect is small. Radiation pressure is unimportant. Outflows are not affected by the radiation feedback.



**Figure 13.** Face-on and edge-on maps of stellar density (left) and total hydrogen column density (right) for the G8 galaxy (baryonic mass of $3.5 \times 10^8$ M$_\odot$) at 250 Myr, with no feedback (top panel), full radiation feedback (middle panel), and added SN feedback (bottom panel). Radiation feedback alone efficiently prevents the formation of massive clumps. SN feedback alone (not shown) has a similar qualitative effect, though it results in a slightly thicker gas disc. Combining the RT and SN feedback smooths the gas distribution further.

qualitative effect as RT feedback only, with the only clear difference being a somewhat thicker gas disc for SN only. Combining RT and SN feedback, however, has some additional impact on the galaxy morphology, with fewer stars and thicker, more diffuse gas disc (bottom panel of Fig. 13).

We compare the star formation rates and outflows for the G8 galaxy in Fig. 14. Here, we see that the star formation rates with RT feedback only are very similar to those in the SN only case. The combination of SN and RT feedback reduces the star formation by about 25 per cent compared to including only one of those processes, which is much less than the relative reduction from the no feedback case when either process was added, which is $\approx 75$ per cent. In Section 3.1.3, we searched qualitatively for the existence of a feedback amplification in the G9 galaxy, i.e. where the addition of one form of feedback (RT) boosts the efficiency of another form (SNe) in quenching star formation, but found no clear evidence. Here, we have an indication of the opposite effect.

The inclusion of direct radiation pressure and dust interactions has no effect on the star formation rate. However, unlike the case of the more massive galaxies, it increases the mass outflow rates non-negligibly, restoring the outflow rate at late times back to that obtained with SN feedback only, as shown by dashed lines in the lower panel of Fig. 14. The effect comes predominantly from direct pressure from the ionizing radiation, as can be seen by comparing the purple and dark red dashed curves.

**Figure 14.** Star formation and outflow rates in the G8 runs with different feedback processes included, as indicated in the legend. Upper panel: stellar mass formed over time. Lower panel: star formation rates (solid lines) and outflow rates across planes at distances of 0.2 $R_{vir}$ from the disc plane (dashed lines). Radiation feedback is as effective as SN feedback at reducing star formation, but does it more smoothly, with SN feedback resulting in more bursty star formation. The relative effect of including a single feedback process (RT or SN) is much stronger than that of adding a second one. Radiation heating dominates the suppression in star formation, and reduces both the outflow rate and the mass loading factor of the outflow. Radiation pressure has a negligible effect on the star formation, but increases the outflow rate during the final ≈250 Myr.

### 3.4 All galaxies: metallicity versus mass

Comparison of the three galaxies in the previous subsections reveals a clear trend: the efficiency of RT feedback decreases with increasing galaxy mass. However, we varied not only the mass, but used a 10 times higher metallicity in the G10 galaxy than in the less massive ones. We now want to investigate how much the RT feedback efficiency is affected by galaxy mass, i.e. the gravitational potential, and how much by the gas metallicity, via its influence on the gas cooling time. For this purpose, we have run the three galaxies at *both* the metallicities we have considered, i.e. 1 Z$_\odot$ and 0.1 Z$_\odot$.

We quantify the efficiency of radiation feedback by calculating the relative reduction of stellar mass formed when a reference simulation is re-run with the addition of full RT feedback, i.e.

$$\zeta^{X}(t) = \frac{M_*(t)^{X+\mathrm{RHPD}}}{M_*(t)^{X}}, \tag{7}$$

where $M_*(t)$ is the stellar mass formed in the simulation up to time $t$ and X represents the feedback included in the reference simulation. Values of $\zeta^{X} < 1$ correspond to feedback which suppresses star formation, while $\zeta^{X} > 1$ indicates *negative* feedback, i.e. enhanced star formation. In Fig. 15, we plot two such RT feedback efficiencies, $\zeta^{\mathrm{NOFB}}$ in the upper panel, which shows the factor by which RT feedback suppresses the stellar mass relative to the simulation
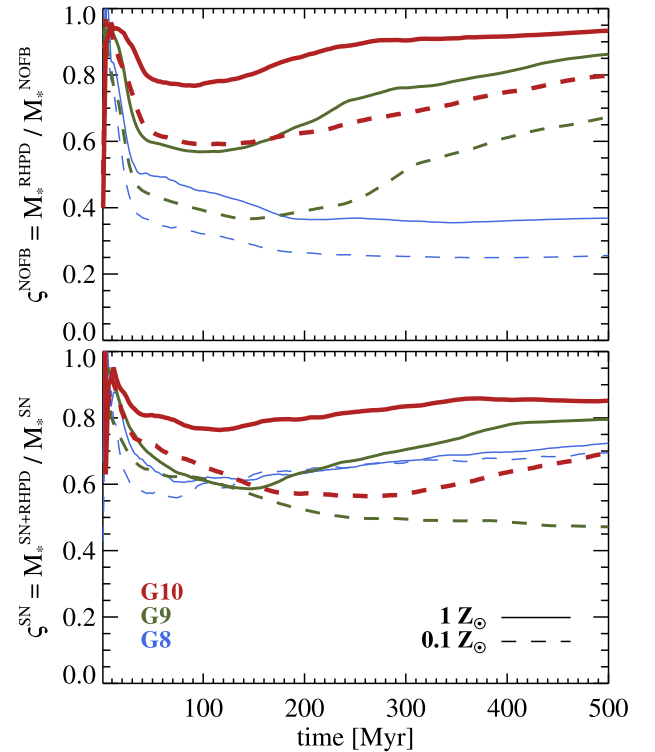


**Figure 15.** RT feedback efficiency, i.e. cumulative suppression of star formation due to RT feedback (RHPD), plotted against time and compared for different galaxy masses and metallicities, as indicated in the legend. Different metallicities are denoted by solid and dashed curves, while galaxy mass is denoted by colour and thickness, with increasing thickness indicating higher mass. An efficiency value of 1 corresponds to no effect on the star formation, while a value close to 0 indicates a strong reduction of the star formation. Upper panel: RT feedback efficiency when acting alone. Lower panel: RT feedback efficiency when combined with SN feedback. Both increased mass and metallicity reduce the efficiency of radiation feedback (and SN feedback, not shown), except if radiation is combined with SN feedback, where the efficiency peaks for the intermediate galaxy mass.

without feedback, and $\zeta^{\mathrm{SN}}$, in the lower panel, which shows the suppression when RT feedback is added to SN feedback.

The upper panel shows the effect of radiation feedback in isolation, and gives a 'cleaner' indication of the feedback efficiency than the lower panel, where the curves are quite sensitive to SN feedback efficiency, which is also (and independently) sensitive to the galaxy mass, metallicity, and stellar particle mass.[3] However, the lower panel is quite important, since the *addition* of radiation to SN feedback is more physically relevant than considering radiation feedback in isolation. We see from both panels that *both* increasing galaxy mass and metallicity weaken the effect of RT feedback (the same applies for SN feedback, though this is not shown in these plots).

The emerging qualitative picture is as follows: star formation in low-mass galaxies is easily regulated by SN feedback, due to a combination of long cooling times (low metallicity and density),

---

[3] Another factor, which we have not considered so far, is the effect that the stellar particle mass has on RT feedback. We have investigated this for one of our galaxies, as discussed in Appendix C. The indication there is that while stellar particle masses have a large effect on the SN feedback efficiency, they have much less impact on the RT feedback, which is likely because the energy injection is smooth rather than instantaneous.

## G10
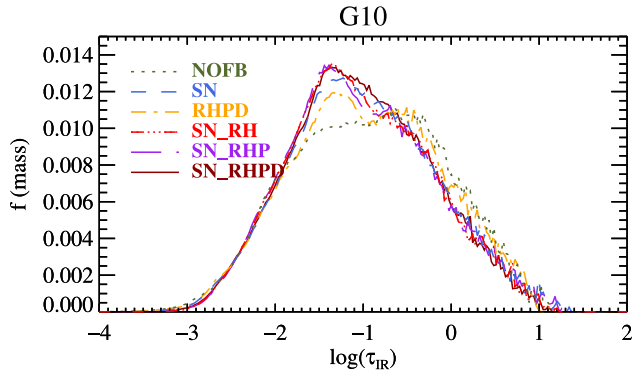


**Figure 16.** Time-stacked mass-weighted probability distribution of IR optical depth, $\tau_{IR}$ along LOSs through the face of the G10 galaxy. The different curves represent inclusion of different feedback processes, as indicated in the legend. A fraction of the gas in this galaxy is in the optically thick regime, $\tau_{IR} > 1$, where multiscattering starts to play a role. However, it has little impact on the galaxy, as can be deduced from the similarity of the optical depth distributions with IR multiscattering pressure excluded and included (purple dot–long-dashed and solid dark red, respectively).

weak gravitational potential, and relatively massive stellar particles. Although RT feedback is by itself roughly as effective at regulating star formation (see Fig. 14), adding it to SN feedback has relatively little effect on the SF regulation, reducing the star formation rate by a few tens of per cent (Fig. 15, lower panel).[4] With increasing galaxy mass, both SN and RT feedback become less effective (Fig. 4 and upper panel of Fig. 15), but combining them may have a larger effect (Fig. 15, lower panel), though this is quite sensitive to the metallicity. At even higher mass, the gravity and cooling has become strong enough that not even the combination of feedback processes can significantly halt the star formation (Figs 12 and 15), especially at the higher, and more realistic, metallicities.

### 3.5 IR multiscattering

The pressure due to multiscattering IR photons has been cited as an important radiation feedback process (Thompson et al. 2005; Murray et al. 2010; Hopkins et al. 2012a,b; Agertz et al. 2013), yet we do not appear do get much of an effect at all from radiation pressure, including that of the IR radiation. In Fig. 16, we show the mass- (or column density-) weighted distributions of LOS IR optical depths, $\tau_{IR}$, through the face of the G10 galaxy, which has the largest optical depths of our discs. The LOSs are taken from time-stacked snapshots (every 50 Myr starting at 100 Myr, as usual), and each has the width of the finest AMR resolution, or 36 pc. The plot quantifies how the mass is distributed in face-on optical depths, which can safely be assumed to be consistently lower than edge-on optical depths, and thus more relevant for estimating the number of scatterings ($\approx \tau_{IR}$) photons typically experience before escaping the disc.

A non-negligible fraction of the gas mass has larger than unity IR optical depths, so radiation trapping and multiscattering does take place in the G10 galaxy, with *maximum* values of $\tau_{IR} \approx 10$. However, as we can clearly see by comparing the curves in Fig. 16, these opacities are not large enough for the IR radiation to diffuse the gas (and hence decrease the optical depths). Due to the lack

of resolution, the gas does not reach the high densities, and hence optical depths, where multiscattering plays a significant role. We can contrast these results to those of Hopkins, Quataert & Murray (2011), where typical optical depths around young stellar particles are found to be much higher, $\sim 10$–$100$, in HD simulations with $\sim$pc resolution.

Murray et al. (2011) argued that the *collective* radiation pressure from star formation can generate cold ($\approx 10^4$ K) outflows. Although our resolution is insufficient to resolve each individual optically thick cloud, we should in principle see this collective large-scale effect in our simulations, but we do not. The Murray et al. (2011) argument applies to massive star-bursting galaxies, and a critical star formation rate surface density of $\dot{\Sigma}_*^{crit} \approx 0.1 \ M_\odot \ yr^{-1} \ kpc^{-2}$. Our galaxies do reach $\dot{\Sigma}_* \sim 10 \ \dot{\Sigma}_*^{crit}$, but this is confined to clumps and centres, with most of the disc below the critical value. However, even if the star formation is mostly below the critical value, we would expect to see some effect of the radiation on outflows, and it is thus interesting that we see no clear effect at all.

Resolution may still be the defining issue though: Murray et al. (2011) envision neutral clouds where the radiative force acts on the surface facing the disc. We do not resolve these dense clouds, and radiation momentum is deposited more smoothly throughout whatever neutral gas exists in the halo. In Section 4.3, we explore qualitatively what we can expect with better resolution, by artificially increasing the IR opacity (but find that outflows are still not generated).
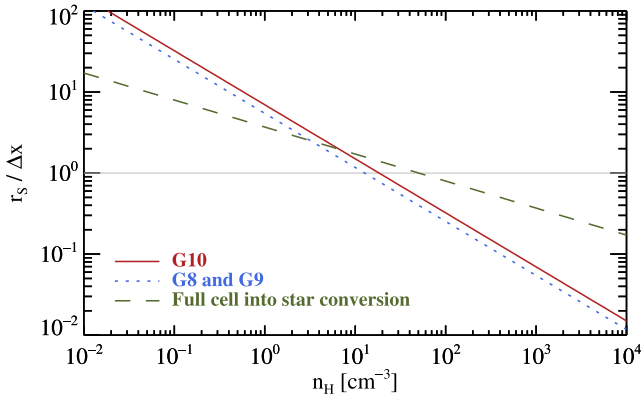
## 4 DISCUSSION

Summarizing the results, we find that radiation feedback has a modest effect on the star formation rates of our simulated galaxies, while outflows are more or less unaffected. The suppression of star formation is due to the suppression of the formation of dense clumps. Radiation feedback becomes less efficient with higher galaxy mass or metallicity, while the combination of radiation and SN feedback appears most effective at intermediate masses (and low densities). Photoionization heating dominates the effect from radiation feedback, while radiation pressure, whether direct or from reprocessed, multiscattering, IR radiation, has a negligible effect.

We will now discuss several aspects of our findings, starting with the apparent inability to resolve H II regions, as implied by Fig. 7. We will then validate our results analytically, comparing the relative impact of the different radiation feedback processes, as expected in the numerical framework. Next, we will consider the expected effect of efficient IR feedback on star formation and outflows by artificially increasing the IR opacity. Finally, we will qualitatively compare our results to previous work on radiation feedback on galaxy scales, where the radiation effect is usually (but not always) modelled with subgrid recipes in pure HD simulations.

### 4.1 On unresolvable H II regions

Our simulations show indications that H II regions are not resolved at gas densities $n_H \gtrsim 10 \ cm^{-3}$ (see Fig. 7 and Section 3.1.3), which potentially affects our results at these high densities. We consider here in detail at what limit H II region resolution becomes an issue.

We can investigate this using the analytic expression for the Strömgren radius of a photoionized region in a uniform medium. The specific ionizing luminosity of stellar sources is $\hat{\mathcal{L}}_{UV} \approx 5 \times 10^{46}$ ionizing photons per second per solar mass, according to the Bruzual & Charlot (2003) model and assuming the Chabrier (2003) IMF (see Fig. A1). A stellar particle of mass $m_*$ then has

---

[4] Hopkins, Quataert & Murray (2012b) find qualitatively similar non-linear effects when combining feedback processes.

**Figure 17.** The plot shows the ratio of the Strömgren radius, $r_S$, of ionized regions versus the maximum cell resolution, $\Delta x = 18$ pc in G8/G9 (dotted blue) and $\Delta x = 36$ pc in G10 (solid red). The H II regions are not resolved above the star formation density threshold ($n_H > 10$ cm$^{-3}$) in our simulations. The dashed green curve shows the ratio, at location of birth, if the total gas mass of a cell is always converted directly into a stellar particle (ignoring the mass depletion of the cell). It demonstrates that with the current star formation method, it is impossible to resolve H II regions above the density threshold for star formation, if this threshold is $\gtrsim 50$ cm$^{-3}$.

luminosity $\hat{L}_{UV} = \hat{\mathcal{L}}_{UV} m_*$ (photons per second). The Strömgren radius around a stellar source is (Strömgren [1939])

$$r_S = \left( \frac{3 \hat{L}_{UV}}{4 \pi \alpha^B n_H^2} \right)^{1/3}$$
$$= 21 \text{ pc}$$
$$\times \left( \frac{\hat{\mathcal{L}}_{UV}}{5 \times 10^{46} \text{ s}^{-1} \text{ M}_\odot^{-1}} \frac{m_*}{600 \text{ M}_\odot} \right)^{1/3} \left( \frac{n_H}{10 \text{ cm}^{-3}} \right)^{-2/3}, \quad (8)$$

where $\alpha^B = 2.6 \times 10^{-13}$ cm$^3$ s$^{-1}$ is the case B recombination rate of hydrogen around $10^4$ K (Ferland et al. [1992]), and where we have substituted the stellar particle mass used in the G8 and G9 simulations, along with the star formation density threshold used in all our simulations. Fig. [17] shows the ratio of the Strömgren radius and the cell width for all three simulated galaxies. For all simulations, the H II regions around young stars are only resolved in gas below the star formation density, $n_*$, and the stars must travel to densities of $n_H \lesssim 1$ cm$^{-3}$ within their 'luminous' lifetime of $\approx 5$ Myr to have their H II regions resolved by more than 10 cell widths.

Judging from equation (8), a simple solution to forcing H II regions to be resolved in AMR simulations would be to increase the mass (and hence luminosity) of the stellar particles. However, unless changes are made to the star formation recipe, we hit a concrete upper limit in $m_*^{max}$, which is the total gas mass of the hosting cell,

$$m_*^{max} = \frac{n_H m_p}{X} (\Delta x)^3 = 1875 \text{ M}_\odot \frac{n_H}{10 \text{ cm}^{-3}} \left( \frac{\Delta x}{18 \text{ pc}} \right)^3, \quad (9)$$

where $X = 0.76$ is the hydrogen mass fraction. Assuming, for arguments sake, that we always convert the total gas mass of cells into stars, and that their neighbourhood has a roughly homogeneous gas density, the ratio of the Strömgren radius and cell width around newly formed stellar particles would be (from equations 8 and 9):

$$\frac{r_S}{\Delta x} = 1.0 \left( \frac{n_H}{50 \text{ cm}^{-3}} \right)^{-1/3}, \quad (10)$$

which is shown by the green dashed curve in Fig. [17]. Even at full gas conversion into stars, H II regions are not well resolved for $n_H \gtrsim 10$ cm$^{-3}$, regardless of the resolution.

So far we assumed that the Strömgren sphere is powered by a single stellar particle. The situation changes when it becomes likely to have multiple young ($\lesssim 5$ Myr) particles in a single cell, increasing the source luminosity and the size of the H II region. From equation (2), we can derive the star formation rate of a cell:

$$\text{SFR}_{\Delta x} = 1.75 \times 10^{-6} \text{ M}_\odot \text{ yr}^{-1}$$
$$\times \left( \frac{\Delta x}{18 \text{ pc}} \right)^3 \left( \frac{\epsilon_{ff}}{0.02} \right) \left( \frac{n_H}{10 \text{ cm}^{-3}} \right)^{3/2}, \quad (11)$$

from which we can then derive the hydrogen number density at which more than one stellar particle, on average, is formed over 5 Myr, the time during which the stellar particles are luminous. This density, at which we can start expecting multiple young stellar particles per cell, is

$$n_H^{mult} = 167 \text{ cm}^{-3} \left( \frac{m_*}{600 \text{ M}_\odot} \right)^{2/3} \left( \frac{\epsilon_{ff}}{0.02} \right)^{-2/3} \left( \frac{\Delta x}{18 \text{ pc}} \right)^{-2}, \quad (12)$$

which coincides roughly with the density at which the track of temperature versus density widens to the right, in the bottom phase diagrams of Fig. [7]. However, the phase diagrams demonstrate that, at the current resolution, the presence of multiple stellar particles in a single cell is insufficient to resolve Strömgren spheres at high densities, as the cells with multiple stellar particles clearly do not reach $T \approx 10^4$ K.

We now see that H II regions *cannot* be fully resolved above these moderately large gas densities, unless changes are made to the star formation recipe, where e.g. more massive stellar particles are formed from gas in a group of neighbouring cells or they are allowed to accrete gas in their lifetime. Stellar particle accretion is usually applied in numerical simulations of protostar formation and the evolution of individual molecular clouds, i.e. simulations at subgalactic scales, and perhaps we are approaching a level of detail which requires some merging of methods for these different scales of galaxy evolution. Alternatively, one could apply stochastic radiation feedback, by allowing on average one in X particles to emit radiation at X times the default luminosity. Such an approach has been used by Dalla Vecchia & Schaye ([2012]) and Roškar et al. ([2014]) for SN feedback to overcome a related resolution problem of overcooling and an oversmooth distribution of stars. Stochastic radiation and SN feedback would thus appear to mesh quite naturally together to overcome resolution problems. This is beyond the scope of this paper though, and we can merely note the limitations in our feedback at high densities, which are in any case close to the resolution limit, where the pressure becomes dominated by the Jeans resolving pressure floor. It is presently unclear what the exact effect of underresolved H II regions is in our simulations, but likely it leads to an underestimate of the effect of photoionization heating, since the gas in underresolved H II regions is heated to an unrealistically low temperature (a fraction of the photoionized temperature which corresponds roughly to the ratio of the size of the real H II region and the cell size).

### 4.2 Analytic comparison of the RT feedback processes

Among the main results of our simulations is that photoionization heating has a modest effect on regulating star formation, while radiation pressure contributes negligibly. We now seek to understand

these results analytically, in order to see if they make physical sense and to ensure that they are not the product of implementation bugs.

We can compare, within our numerical framework, the efficiencies of the different radiation feedback processes, i.e. photoionization heating, direct pressure from ionizing photons, direct pressure from optical photons, and multiscattering pressure from IR photons. To simplify and quantify this comparison, we consider feedback in a single cell containing a radiation source and ignore radiation entering the cell from the outside. While we will write the following equations in terms of the simulation cell size, $\Delta x$, and the mass of stellar particles, $m_*$, most of the equations also hold approximately for gas at a distance $\sim \Delta x$ from a star (cluster) of mass $m_*$ with the assumed (and theoretically motivated) specific luminosity, provided the density, temperature, and metallicity are nearly uniform within $\Delta x$.

We compare the radiation feedback efficiencies in terms of approximate 'effective' temperatures. For photoionization heating, this is equal to the temperature of gas photoionized by stars, while for direct and IR radiation pressure (with the motivation of comparing those processes in a simple way), it is defined by equating the radiation pressure and the thermal pressure.

### 4.2.1 Photoionization heating

Photoionization tends to heat the ionized gas to $T_{\mathrm{H\,II}} \approx 2 \times 10^4$ K, as we have seen in Fig. 7. If the Strömgren radius extends outside the cell, then the cell is simply heated to $T_{\mathrm{H\,II}}$, otherwise it is heated to a fraction of that temperature which reflects the ratio of the volume of the Strömgren sphere to that of the cell, i.e. the host cell is heated to

$$T^{\mathrm{PH}} \sim 2 \times 10^4 \text{ K} \times \min\left(f_{\mathrm{vol}},\ 1\right), \tag{13}$$

where

$$f_{\mathrm{vol}} = \frac{\frac{4}{3}\pi r_{\mathrm{S}}^3}{(\Delta x)^3} = 6.7 \frac{\hat{\mathcal{L}}_{\mathrm{UV}}}{5 \times 10^{46} \text{ s}^{-1} \mathrm{M}_\odot^{-1}} \frac{m_*}{600 \text{ M}_\odot}$$
$$\times \left(\frac{n_{\mathrm{H}}}{10 \text{ cm}^{-3}}\right)^{-2} \left(\frac{\Delta x}{18 \text{ pc}}\right)^{-3}, \tag{14}$$

and we substituted our (G8 and G9) simulation parameters for $\Delta x$, $\hat{\mathcal{L}}_{\mathrm{UV}}$, and $m_*$ (and the star formation threshold for $n_{\mathrm{H}}$). The specific stellar population luminosity, for the UV and for the other photon groups, can be read (approximately) from Fig. A1.

### 4.2.2 Direct pressure from photoionization

To quantify the effect of radiation pressure and compare it to photoionization heating, we measure it in terms of an effective temperature, corresponding to the pressure applied via momentum absorption from the radiation, and defined as

$$T_{\mathrm{Eff}} \equiv \frac{P_{\mathrm{rad}} m_{\mathrm{p}}}{\rho k_{\mathrm{B}}}. \tag{15}$$

The radiation pressure is roughly the momentum absorption rate in the cell, $\dot{p}$ (momentum per unit time), divided by the cell area,

$$P_{\mathrm{rad}} = \frac{\dot{p}}{6(\Delta x)^2}. \tag{16}$$

The momentum absorption rate can be estimated from the luminosity of the stars contained in the cell and the opacity of the cell gas. The effective temperature is approximate, because we neglect the dependence on the mean gas particle mass $\mu$, and we assume the radiation pressure to be isotropic.

We assume for simplicity that the cell gas is in photoionization equilibrium with the emitted radiation,[5] and we ignore the radial dependence of the neutral fraction inside resolved H II regions. We can then use the size of the predicted H II region, given by equation (8), to estimate the fraction of the ionizing luminosity contributing to the direct radiation pressure in the emitting cell, giving

$$T_{\mathrm{Eff}}^{\mathrm{UV}} \sim \frac{L_{\mathrm{UV}}}{c} \frac{1}{6(\Delta x)^2} \frac{m_{\mathrm{p}}}{\rho k_{\mathrm{B}}} \times \min\left(f_{\mathrm{vol}}^{-1},\ 1\right)$$
$$\sim 1.2 \times 10^3 \text{ K} \frac{\mathcal{L}_{\mathrm{UV}}}{2 \times 10^{36} \text{ erg s}^{-1} \mathrm{M}_\odot^{-1}} \frac{m_*}{600 \text{ M}_\odot}$$
$$\times \left(\frac{n_{\mathrm{H}}}{10 \text{ cm}^{-3}}\right)^{-1} \left(\frac{\Delta x}{18 \text{ pc}}\right)^{-2} \times \min\left(f_{\mathrm{vol}}^{-1},\ 1\right), \tag{17}$$

where we now measure the luminosity (and specific), $L_{\mathrm{UV}}$ ($\mathcal{L}_{\mathrm{UV}}$), in terms of energy rather than photon count (the value is again typical for the SED model utilized). The rightmost term accounts for whether the H II region is resolved or not: the fraction of the ionizing luminosity pressurising the emitting cell is the volume of the H II region over that of the cell, but this fraction is roofed at unity, meaning all the emitted photons are absorbed in the emitting cell as the H II region becomes unresolved.

### 4.2.3 Pressure on dust from optical photons

The effective temperature corresponding to the pressure on gas via dust from optical photons is

$$T_{\mathrm{Eff}}^{\mathrm{Opt}} \sim \frac{L_{\mathrm{Opt}}}{c} \frac{1}{6(\Delta x)^2} \frac{m_{\mathrm{p}}}{\rho k_{\mathrm{B}}} \ (1 - e^{-\tau_{\mathrm{Opt}}})$$
$$\sim 1.8 \times 10^3 \text{ K} \frac{\mathcal{L}_{\mathrm{Opt}}}{3 \times 10^{36} \text{ erg s}^{-1} \mathrm{M}_\odot^{-1}} \frac{m_*}{600 \text{ M}_\odot}$$
$$\times \left(\frac{n_{\mathrm{H}}}{10 \text{ cm}^{-3}}\right)^{-1} \left(\frac{\Delta x}{18 \text{ pc}}\right)^{-2} (1 - e^{-\tau_{\mathrm{Opt}}}), \tag{18}$$

where $\tau_{\mathrm{Opt}}$ is the optical depth of the host cell:

$$\tau_{\mathrm{Opt}} \sim \kappa_{\mathrm{Opt}} \rho \Delta x$$
$$\sim 1.2 \frac{\tilde{\kappa}_{\mathrm{Opt}}}{10^3 \text{ cm}^2 \text{ g}^{-1}} \frac{Z}{Z_\odot} \frac{n_{\mathrm{H}}}{10 \text{ cm}^{-3}} \frac{\Delta x}{18 \text{ pc}}. \tag{19}$$

We ignore pressure on dust from UV photons, because the pressure from the UV photons is already counted, in $T_{\mathrm{Eff}}^{\mathrm{UV}}$, for photoionization, for which the opacity is orders of magnitude higher than for dust absorption.

### 4.2.4 Multiscattering pressure on dust from IR photons

The effective temperature for multiscattering reprocessed IR photons is

$$T_{\mathrm{Eff}}^{\mathrm{IR}} \sim \frac{L_{\mathrm{IR}}}{c} \frac{1}{6(\Delta x)^2} \frac{m_{\mathrm{p}}}{\rho k_{\mathrm{B}}} \tau_{\mathrm{IR}} = \frac{L_{\mathrm{IR}}}{c} \frac{\kappa_{\mathrm{IR}} m_{\mathrm{p}}}{6 \Delta x k_{\mathrm{B}}}$$
$$\sim 22 \text{ K} \frac{\mathcal{L}_{\mathrm{Opt}}}{3 \times 10^{36} \text{ erg s}^{-1} \mathrm{M}_\odot^{-1}} \frac{m_*}{600 \text{ M}_\odot}$$
$$\times \frac{\tilde{\kappa}_{\mathrm{IR}}}{10 \text{ cm}^2 \text{ g}^{-1}} \frac{Z}{Z_\odot} \left(\frac{\Delta x}{18 \text{ pc}}\right)^{-1}. \tag{20}$$

---

[5] We ignore the instantaneous pressure from the radiation when the cell is in the process of being ionized, leading us to underestimate the direct pressure at low densities, where growing H II regions are resolved.

We only consider the optical stellar luminosity, since the IR luminosity is negligible in comparison (see Fig. A1). The IR multiscattering feedback depends on the optical photons being absorbed and re-emitted into the IR. It is a safe assumption though, that this is true under any circumstances where multiscattering is important, since $\kappa_{\rm IR} \ll \kappa_{\rm Opt}$.

The expression for the IR effective temperature assumes trapping of photons originating *within* the cell and ignores additional trapping of photons originating from the neighbouring environment. The previous expression should therefore be taken as a lower limit. This is less of a concern for the other radiation feedback processes, since they are unresolved at high (star-forming) densities, and we thus expect much less intercell flux of photons.

### 4.2.5 Relative impact of the radiation feedback processes

To compare the radiation feedback processes (equations 13–20), we replace the stellar mass, $m_*$, by the fraction $f_* \leq 1$ of the gas mass in a cell at a given density and volume. The value $f_* = 1$ gives an approximate upper limit on the effective temperature estimates for each of the processes, with the possible exception of the IR radiation, where things are more uncertain, as argued in the previous subsection. We thus assume

$$m_* = f_* \frac{n_{\rm H} m_{\rm p}}{X} (\Delta x)^3 = 1875\,{\rm M_\odot}\; f_* \frac{n_{\rm H}}{10\,{\rm cm^{-3}}} \left(\frac{\Delta x}{18\,{\rm pc}}\right)^3. \quad (21)$$

In practice, the mass of each stellar particle is some fraction (1/3 in the G8 and G9 simulations, 2/3 in G10) of the cell gas mass at the density threshold for star formation. The upper limit we use in equation (21), reflects the fact that at large densities, multiple stellar particles can be expected to form in the same cell over a short time-scale, but no more than the total gas mass in a cell can be converted into stars.

Substituting equation (21) into equations (13)–(20) gives

$$T^{\rm PH} = 2 \times 10^4\,{\rm K} \times \min\left(f_{\rm vol},\, 1\right), \quad (22)$$

$$T^{\rm UV}_{\rm Eff} = 3.7 \times 10^3\,{\rm K}\, \frac{\mathcal{L}_{\rm UV}}{2 \times 10^{36}\,{\rm erg\,s^{-1}\,M_\odot^{-1}}} \frac{\Delta x}{18\,{\rm pc}}$$
$$\times \min\left(f_{\rm vol}^{-1},\, 1\right)\, f_*, \quad (23)$$

$$T^{\rm Opt}_{\rm Eff} = 5.6 \times 10^3\,{\rm K}\, \frac{\mathcal{L}_{\rm Opt}}{3 \times 10^{36}\,{\rm erg\,s^{-1}\,M_\odot^{-1}}} \frac{\Delta x}{18\,{\rm pc}}$$
$$\times \left(1 - e^{-\tau_{\rm Opt}}\right)\, f_*, \quad (24)$$

$$T^{\rm IR}_{\rm Eff} = 69\,{\rm K}\, \frac{\mathcal{L}_{\rm Opt}}{3 \times 10^{36}\,{\rm erg\,s^{-1}\,M_\odot^{-1}}} \frac{\tilde{\kappa}_{\rm IR}}{10\,{\rm cm^2\,g^{-1}}} \frac{Z}{Z_\odot}$$
$$\times \frac{n_{\rm H}}{10\,{\rm cm^{-3}}} \left(\frac{\Delta x}{18\,{\rm pc}}\right)^2 f_*, \quad (25)$$

where the volume fraction,

$$f_{\rm vol} = \left(\frac{n_{\rm H}}{2.1 \times 10^2\,{\rm cm^{-3}}}\right)^{-1} \frac{\hat{\mathcal{L}}_{\rm UV}}{5 \times 10^{46}\,{\rm s^{-1}\,M_\odot^{-1}}}\, f_*, \quad (26)$$

is independent of resolution.

These effective temperatures are plotted in Fig. 18, for $f_* = 1$ and $Z = Z_\odot$, with the thick curves representing the 18 pc resolution used for our lower mass galaxies, and the thin curves corresponding
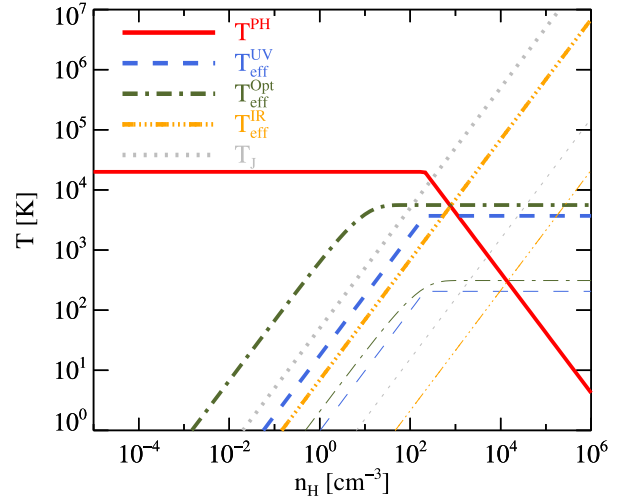


**Figure 18.** Effective temperatures acquired in a single emitting cell via the different radiation feedback processes (equations 22–25), assuming $Z = Z_\odot$ and that a fraction $f_* = 1$ of the cell gas is converted instantaneously into stars. For the thick lines, we assume $\Delta x = 18$ pc, while for the thin lines we assume 1 pc resolution. The processes considered are as follows: photoionization heating (solid red), direct pressure from photoionization (dashed blue), direct pressure via dust from optical photons (dot–dashed green), and multiscattering pressure from IR photons (triple-dot–dashed yellow). Also plotted, in dotted grey, is the effective temperature of the density-dependent pressure floor (equation 5). Photoionization heating dominates the radiation feedback at low densities in this single cell limit, while the pressure floor takes over at high densities. The first-order effect of increasing the resolution is to decrease the effect of radiation pressure. However, at extreme densities, IR trapping by multiple stellar particles on scales larger than the cell width is likely to give a boost over that indicated in the plot.

to $\Delta x = 1$ pc. We also plot (in dotted grey) the artificial non-thermal pressure, equation (5), that is imposed to resolve the Jeans scales, and we shift it with resolution according to equation (4).

Photoionization heating (solid red) dominates at low densities, $n_{\rm H} \lesssim 10^2\,{\rm cm^{-3}}$, heating the gas to $\approx 2 \times 10^4$ K, while for higher densities, radiation feedback is surpassed by the Jeans pressure. In the absence of the Jeans pressure, IR multiscattering would dominate at high densities. The direct UV and optical radiation effective temperatures plateau at high densities, as the total particle luminosity becomes absorbed in the local cell, and increasing the resolution only makes radiation pressure weaker, since the lower stellar mass (and hence luminosity) has a stronger negative effect ($\propto (\Delta x)^3$) compared to the positive effect of the decreased cell area ($\propto (\Delta x)^{-2}$). The IR radiation pressure is the only term which keeps rising for increasing densities, which is due to the multiscattering, and it dominates over other radiation feedback processes at extreme densities. The IR effective temperature is, however, lower than the artificial pressure floor, $T_{\rm J}$, by about an order of magnitude (at $Z = Z_\odot$), at any resolution.

Fig. 18 qualitatively justifies the results of our simulations. Comparing the plot to the bottom right phase diagram of Fig. 7, the plateau of $\approx 2 \times 10^4$ K gas is clear in both figures, and the drop-off in temperature, which is a manifestation of unresolved H II regions, occurs at a similar density, though slightly lower in the phase diagram, which is because less than the full cell mass is converted into stars in the simulations ($f_* = 1/3$). Radiation (heating) feedback is effective in preventing gas at low densities from clumping, but futile in dispersing clouds once the densities become high. Radiation

pressure vanishes at low densities, and is negligible compared to the artificial Jeans pressure at high densities.

Judging from Fig. 18, it appears that the modelled radiation pressure is doomed to always remain weaker than the artificial pressure floor we are forced to apply, especially considering that we are assuming an extreme upper limit where the full gas mass in a cell is converted instantaneously into stars. However, we stress again that we only consider in this analysis the effect in a single cell, and ignore the effect appearing from external stellar populations in neighbouring cells (and we also ignore the fact that particles can move to higher or lower densities during their lifetime). We can conclude that direct radiation pressure is weak at any resolution, but with many stellar particles forming in highly resolved optically thick regions, we may see a considerable boost in the pressure from trapped multiscattering IR radiation with higher resolution (and only at high densities). It remains a task for future work to establish what kind of resolution is required to see such a boost, but in the next subsection we will investigate what effects we can expect from it on large scales.

The above analysis does not apply to the time-integrated effect of collective, direct long-range radiation pressure from many stellar populations on galactic scales, e.g. in stirring diffuse gas or pushing cold clouds out of the galaxy (Murray et al. 2011). However, this effect is unimportant in our simulated galaxies, since it exists (and is in fact exaggerated due to our full reduced flux approximation), yet radiation feedback is dominated by heating, with radiation pressure at best having a marginal impact.

## 4.3 What does it take for IR radiation pressure to dominate, and what happens then?

Up to this point, we have found that IR radiation has only a marginal effect on our galaxies, and we have shown analytically that these results are to be expected with our current model and resolution. The considerable increase in resolution, that appears to be required to investigate IR pressure feedback on small scales, and possible cascading effects on larger scales, is beyond our reach in this paper. We can, however, instead artificially allow the IR radiation to dominate the galactic feedback by simply increasing the IR opacity. This can give us an estimate of how far we are from efficient IR feedback, and, more importantly, how the galaxy reacts when IR feedback does become efficient on small scales. Thus, we get an idea about what to expect *if* we resolve the very large optical depths that are required for multiscattering radiation pressure to play a role. For example, does the radiation generate large-scale winds, and does it create a much thicker gas or stellar disc? We thus ran variants of the G10_RHPD simulation (where the IR optical depths are largest) with increased IR opacities. We compare here results for $\tilde{\kappa}_{IR} = (10^2, 10^3, 10^4) \, \text{cm}^2 \, \text{g}^{-1}$, i.e. ten, a hundred and a thousand times the default, physically motivated, opacity that we have used so far. We also set $\tilde{\kappa}_{UV} = \tilde{\kappa}_{Opt} = \tilde{\kappa}_{IR}$ in the highest opacity run in order to increase the IR reproduction from higher energy photons in line with the opacity increase.

Fig. 19 shows star formation rates and outflow rates across planes $0.2 \, R_{vir}$ from the disc plane. We hardly see any effect on the star formation rate, though the outflow rate is slightly reduced. Further increased opacity increasingly suppresses both star formation and outflow rates, with a very bursty star formation and almost totally quenched outflows in the most extreme case. The reduction in the outflow rate, which is at least as large as for the SFR, even with the appearance of bursty star formation, strengthens the impression of
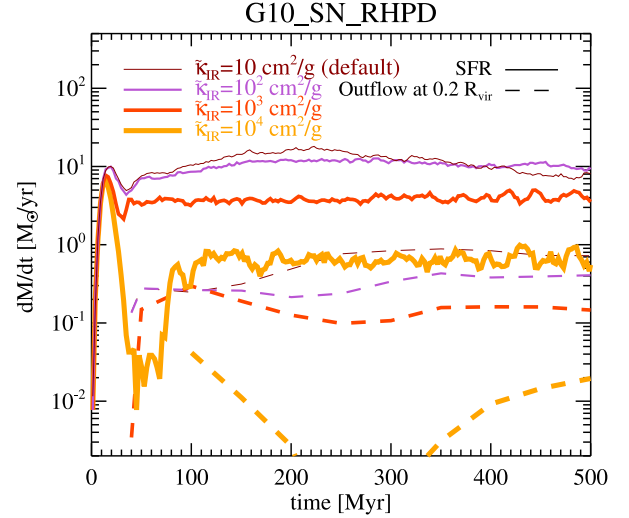


**Figure 19.** Star formation rates (solid lines) and outflow rates across planes at distances of $0.2 \, R_{vir}$ from the disc plane (dashed lines) in the G10_SN_RHPD galaxy with increased IR opacity. The thinnest (dark red) curve shows the results for the default opacity that we have used so far and the successively thicker curves show results where the IR opacity is increased, each time by a factor of 10. The star formation becomes bursty in the case with the highest opacity. Outflow rates decrease with increasing opacity, more or less in line with the reduced star formation, indicating that the radiation disrupts star-forming clouds gently, rather than violently.
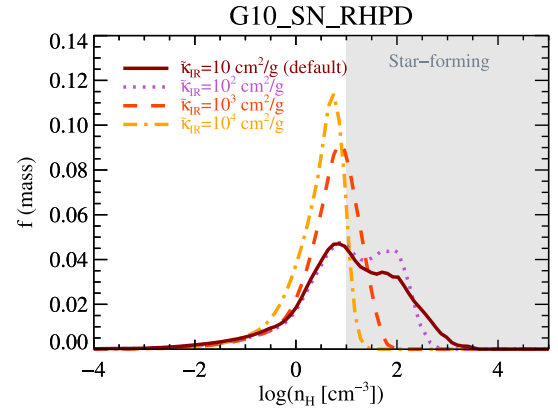


**Figure 20.** Time-stacked mass-weighted gas density distribution in the G10_SN_RHPD galaxy, with increasing IR opacity. For the highest opacity used, when the star formation is reduced by more than an order of magnitude, the density distribution becomes cuts off at the star formation threshold, $n_H = 10 \, \text{cm}^{-3}$.

a non-violent radiation feedback, which stirs up the gas but does not systematically eject it.

Fig. 20 shows the effect of the increased opacities on the gas density distribution. As expected, the IR radiation suppresses high densities more efficiently with increased opacity. For the highest opacity, the density distribution cuts off at the star formation density threshold ($n_* = 10 \, \text{cm}^{-3}$). This indicates that the IR pressure does indeed become very efficient at preventing gas to form stars, but that is more or less the whole effect, i.e. the gas is kept diffuse, but within the galaxy. The IR pressure shifts SN explosions to lower densities, but this does not lead to increased outflow rates, as the reduced star
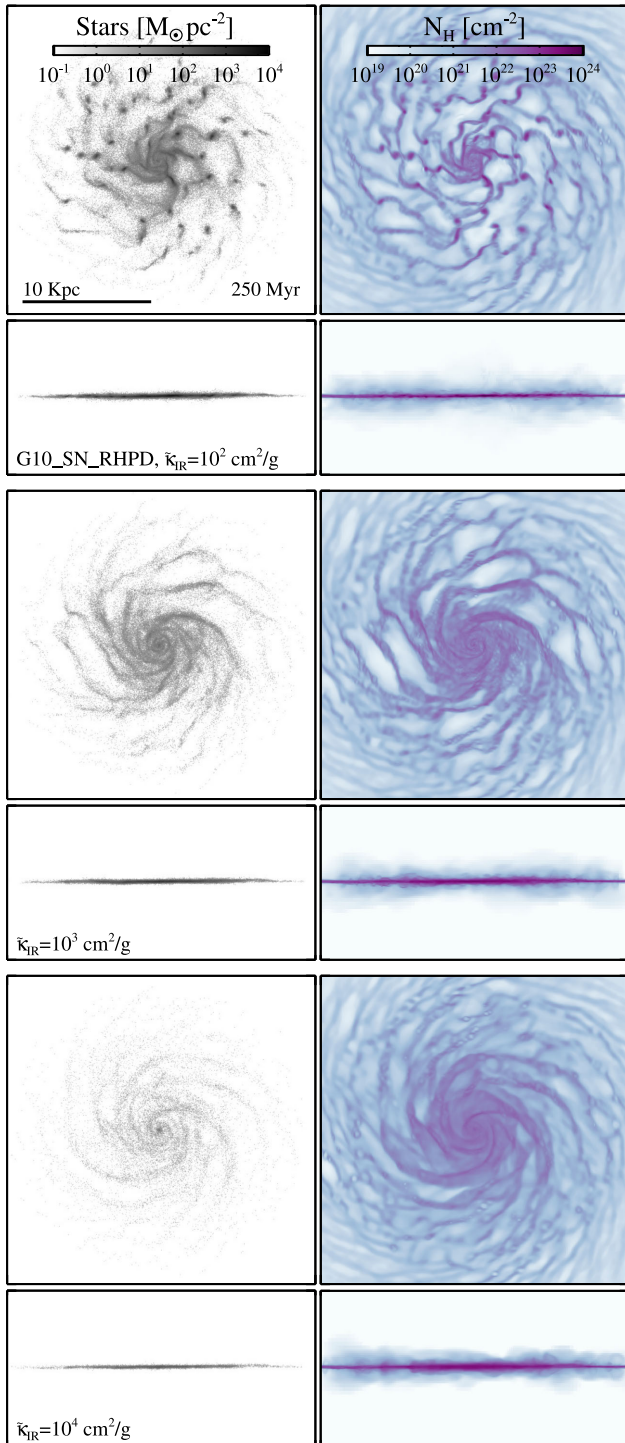
**Figure 21.** Maps of the G10 galaxy ($3.5 \times 10^{10}$ M$_\odot$ in baryons) at 250 Myr, for SN and full RT feedback (same as bottom-left panel in Fig. 11), but with increased IR opacity, as indicated in each panel: the opacities are increased from the default by a factor 10 (top), $10^2$ (middle), and $10^3$ (bottom). The increased dominance of IR radiation pressure simply has the effect of smoothing out the peaks in gas density, and suppressing star formation.

formation more than compensates to reduce the outflows, leading to a decrease in mass loading with increasing opacity.

Finally, we compare the galaxy morphologies for the different opacity values in Fig. 21. The galaxy simply becomes smoother with increasing opacity, both in the gas and stars.

## 4.4 Comparison with other work

While many studies exist in the literature where radiation feedback (on galactic scales) is modelled with subgrid recipes in pure HD simulations, there are only a few in which a subset of the radiation feedback mechanisms that are modelled here are studied with RHD (Petkova & Springel 2011; Wise et al. 2012a; Hasegawa & Semelin 2013; Kim et al. 2013; Pawlik, Schaye & Dalla Vecchia 2015; Pawlik, Milosavljević & Bromm 2013).

In cosmological simulations of reionization-era galaxy formation, Wise et al. (2012a) found direct radiation pressure to play a major role, suppressing star formation strongly and boosting outflow rates, but did not report on the isolated effect of photoionization heating, which was always included, and they did not include IR radiation effects (which are likely weak in such metal-poor galaxies). Petkova & Springel (2011), Hasegawa & Semelin (2013), Pawlik et al. (2013) also modelled reionization-era galaxies, but only included radiation heating. They all found that radiation heating gently suppressed star formation, while they did not report on boosted outflows. Pawlik et al. (2015) considered the addition of SN feedback and found that it dominated over the effect of radiation heating on star formation histories. Kim et al. (2013) used the RHD implementation from Wise et al. (2012a) on an isolated $\sim$ MW mass galaxy, and found slight ($\sim$20 per cent) suppression of star formation, which they attributed to radiation heating, rather than radiation pressure.

A large amount of work exists where radiation feedback has been included in pure HD simulations in the form of subgrid recipes, which are often empirically motivated. Although there are quantitative, and sometimes qualitative, differences, these studies broadly agree that IR radiation pressure strongly suppresses star formation and generates (sometimes extremely massive) outflows (e.g. Hopkins et al. 2011, 2012a,b,c; Agertz et al. 2013; Aumer et al. 2013; Stinson et al. 2013; Agertz & Kravtsov 2015; Roškar et al. 2014). There are exceptions though: Ceverino et al. (2014) and Moody et al. (2014) found direct radiation pressure to mildly suppress star formation, while radiation heating and IR radiation pressure had a negligible effect. Trujillo-Gomez et al. (2015), on the other hand, found radiation heating dominated over direct radiation pressure in suppressing star formation, while outflows were not affected by the radiation (and IR effects were not considered).

Our results do not show a wide and general agreement with previous studies of the effects of radiation feedback on galactic scales, which is not surprising, since there is no general agreement in the literature. The discrepancies probably largely come down to resolution. It appears that both RHD and HD simulations that show a substantial effect from IR radiation pressure have either sub-pc resolution or a subgrid model that boosts the optical depths. We lack sub-pc resolution in this paper, and we have so far made no attempt to compensate this with a subgrid model. Of these two options, we prefer in future work to increase the resolution, to probe from first principles how radiation feedback affects small scales, and how this effect may (or may not) cascade to larger scales. The strongest general disagreement we can find with other work concerns outflows. Where they are studied in the literature, radiation feedback appears to boost outflows most of the time, which is in contrast with our simulations. Our experiments with boosted IR radiation opacities hint that increased resolution will still leave us with a lack of radiation-generated outflows, but in the end, the best way to find out is to actually increase the resolution.

# 5 CONCLUSIONS AND FUTURE WORK

We ran and analysed AMR simulations of isolated disc galaxies of baryonic masses $3.5 \times (10^8, 10^9, 10^{10}) \, M_\odot$ (the largest mass being comparable to that of the Milky Way), using a maximum resolution of 18 pc. We studied the effects or stellar radiation feedback, which was modelled with RHD, acting on its own and also combined with ('thermal dump') SNe feedback. We compared the effects of three separate radiation feedback processes: photoionization heating, direct radiation pressure from UV, and optical photons, and pressure from multiscattered, reprocessed IR radiation. These are the first galaxy-scale simulations which model all these processes concurrently and with RHD. Our main findings are the following:

(i) Stellar radiation feedback suppresses star formation in the simulated galaxies. It does so predominantly by preventing the formation of star-forming clumps, rather than by destroying those that form. The suppression of star formation with radiation feedback (ranging from a factor of 4 for the low-mass galaxy to only $\sim 0.1$ for the most massive one) is similar to that of 'thermal dump' SN feedback.

(ii) Radiation feedback does not significantly amplify the efficiency of SN feedback, and in fact there is a hint of the opposite effect in the lowest mass galaxy we consider, where the combination of radiation and SN feedback results in a weaker star formation suppression than one would naively expect from multiplying the individual suppression factors, although the combined effect does exceed that of the individual feedback processes.

(iii) Radiation feedback has a negligible effect on galaxy outflows. If anything, the outflow rates are slightly suppressed, owing to the reduced star formation and subsequent decrease in SN activity. The outflow mass loading factor, i.e. the ratio between the outflow rate and the star formation rate, is typically of the order of $10^{-1}$, which is very low compared to non-RHD simulations that use subgrid recipes for radiation feedback (e.g. Hopkins et al. 2012b).

(iv) As with ('thermal dump') SN feedback, the effect of radiation feedback on star formation weakens with galaxy mass and metallicity. The combined effect of SN and radiation feedback is strongest in our intermediate-mass galaxy, which has a baryonic mass of $3.5 \times 10^9 \, M_\odot$, i.e. about one-tenth of the mass of our MW.

(v) The dominant form of radiation feedback is photoionization heating, while the effect of radiation pressure, both direct and on dust, is borderline negligible. We are able to explain the relative efficiencies of the different radiation feedback processes using simple analytic estimates within the context of our numerical models.

(vi) The analytic estimates suggest that the effect of direct radiation pressure from ionizing radiation on galaxies is likely negligible in reality. However, multiscattering radiation pressure from IR radiation is not properly captured in our simulations. This is because our resolution ($\sim 10$ pc) does not allow the collapse to sufficiently large local densities for the gas to become significantly optically thick to the IR radiation.

(vii) To estimate the qualitative effects of multiscattering IR radiation that may be revealed by future, higher resolution, simulations, we ran simulations in which the IR opacities were boosted by orders of magnitude over realistic, physically motivated, values. This boost makes multiscattering radiation effective at regulating star formation, but in a gentle way that merely smooths out the galaxy disc, without generating outflows.

(viii) Resolution is also an issue for the ionizing radiation. With the current method for forming stars, where stellar population particles are instantaneously formed out of the gas in a single AMR cell, H II regions are unresolved at densities $n_H \gtrsim 10 \, cm^{-3}$, *regardless of the numerical resolution*. The consequence of the unresolved H II regions is likely an underestimate of the regulating effect of radiation heating on star formation in dense gas, since the gas cells hosting young stars are heated to temperatures lower than the ionization temperature. Possible ways to deal with this problem in the future include stochastic radiation feedback or a modified method for star formation.

(ix) Although we have not considered this in detail, we find in the resolution tests described in Appendix C that radiation feedback is much less sensitive to the stellar particle mass than is ('thermal dump') SN feedback. This makes sense, since the radiation is continuous, while the SNe are instantaneous, and for explosive feedback the radiative losses decrease for higher maximum temperatures.

An important caveat for our study is that our simulated galaxies do not have the high surface densities that occur in the massive, star-bursting galaxies that have been the focus of theoretical work which predicts efficient regulation of star formation and outflows by radiation pressure (e.g. Murray et al. 2011). At high redshift ($z \sim 3$), where gas accretion and star formation peak, radiation pressure may even play a role in 'normal' low-mass galaxies. In the future, we will expand our simulations to include more massive galaxies, and gas-rich galaxies representative of high redshift, which may exhibit greater sensitivity to radiation pressure.

We also note that the choice of SN feedback recipe likely affects the interplay of feedback processes and the net effect of radiation feedback. For simplicity, and in order to make sure we did not overinject feedback energy in this first round of simulations, we used 'thermal dump' SN feedback, which is known to be inefficient and suffer from resolution-induced overcooling. In future studies, it will be interesting to see how the interplay of feedback processes is affected by the use of more efficient (and more realistic) SN feedback recipes.

There are many additional interesting paths to follow, such as improvements of our radiation feedback model, the inclusion of other sources of radiation than stars, and an expansion to both larger and smaller physical scales.

An interesting model improvement is to consider the effect of the local radiation field on metal cooling, which has been suggested by Cantalupo (2010) to effectively quench cooling and subsequently star formation in galaxies. Another important model improvement is the inclusion of the formation and radiative dissociation of $H_2$, which is highly relevant for studying star formation in detail. AGN feedback may be fundamentally radiative in origin, and it is quite interesting to see in what ways, if any, RHD experiments would differ from subgrid recipes. It is relatively straightforward to add AGN radiation to our simulations, as long as a recipe for black hole accretion is in place. Some additional radiation processes, such as Compton scattering, are likely important, and it is quite likely that it will remain difficult to resolve optically thick regions properly.

We intend to study radiation feedback on scales both larger and smaller than this study. The larger scales involve cosmological zoom RHD simulations, where the effect of radiation feedback can be studied in galaxies that evolve in their natural environment, and we can study the effect on galaxy evolution, inflows, outflows, and the observable properties of the ISM and CGM. Going to smaller scales will allow us to properly resolve optically thick star-forming clouds and how they are affected by stellar.

## REFERENCES

Agertz O., Kravtsov A. V., 2015, ApJ, 804, 18
Agertz O., Kravtsov A. V., Leitner S. N., Gnedin N. Y., 2013, ApJ, 770, 25
Aumer M., White S. D. M., Naab T., Scannapieco C., 2013, MNRAS, 434, 3142
Binney J., 1977, ApJ, 215, 483
Booth C. M., Schaye J., 2009, MNRAS, 398, 53
Bower R. G., Benson A. J., Malbon R., Helly J. C., Frenk C. S., Baugh C. M., Cole S., Lacey C. G., 2006, MNRAS, 370, 645
Brook C. B., Stinson G., Gibson B. K., Wadsley J., Quinn T., 2012, MNRAS, 424, 1275
Bruzual G., Charlot S., 2003, MNRAS, 344, 1000
Cantalupo S., 2010, MNRAS, 403, L16
Ceverino D., Klypin A., Klimek E. S., Trujillo-Gomez S., Churchill C. W., Primack J., Dekel A., 2014, MNRAS, 442, 1545
Chabrier G., 2003, PASP, 115, 763
Creasey P., Theuns T., Bower R. G., Lacey C. G., 2011, MNRAS, 415, 3706
Creasey P., Theuns T., Bower R. G., 2013, MNRAS, 429, 1922
Dalla Vecchia C., Schaye J., 2012, MNRAS, 426, 140
Di Matteo T., Springel V., Hernquist L., 2005, Nature, 433, 604
Dubois Y., Devriendt J., Slyz A., Teyssier R., 2010, MNRAS, 409, 985
Ferland G. J., Peterson B. M., Horne K., Welsh W. F., Nahar S. N., 1992, ApJ, 387, 95
Ferland G. J., Korista K. T., Verner D. A., Ferguson J. W., Kingdon J. B., Verner E. M., 1998, PASP, 110, 761
Geen S., Rosdahl J., Blaizot J., Devriendt J., Slyz A., 2015, MNRAS, 448, 3248
Gnedin N. Y., Abel T., 2001, New Astron., 6, 437
Haardt F., Madau P., 1996, ApJ, 461, 20
Hasegawa K., Semelin B., 2013, MNRAS, 428, 154
Hopkins P. F., Quataert E., Murray N., 2011, MNRAS, 417, 950
Hopkins P. F., Quataert E., Murray N., 2012a, MNRAS, 421, 3488
Hopkins P. F., Quataert E., Murray N., 2012b, MNRAS, 421, 3522
Hopkins P. F., Kereš D., Murray N., Quataert E., Hernquist L., 2012c, MNRAS, 427, 968
Hopkins P. F., Kereš D., Oñorbe J., Faucher-Giguère C.-A., Quataert E., Murray N., Bullock J. S., 2014, MNRAS, 445, 581
Kannan R. et al., 2014a, MNRAS, 437, 2882
Kannan R., Stinson G. S., Macciò A. V., Brook C., Weinmann S. M., Wadsley J., Couchman H. M. P., 2014b, MNRAS, 437, 3529
Katz N., 1992, ApJ, 391, 502
Kim J.-h., Krumholz M. R., Wise J. H., Turk M. J., Goldbaum N. J., Abel T., 2013, ApJ, 779, 8
Kim J.-h. et al., 2014, ApJS, 210, 14
Li A., Draine B. T., 2001, ApJ, 554, 778
Moody C. E., Guo Y., Mandelker N., Ceverino D., Mozena M., Koo D. C., Dekel A., Primack J., 2014, MNRAS, 444, 1389
Moster B. P., Naab T., White S. D. M., 2013, MNRAS, 428, 3121
Murray N., Quataert E., Thompson T. A., 2005, ApJ, 618, 569
Murray N., Quataert E., Thompson T. A., 2010, ApJ, 709, 191
Murray N., Ménard B., Thompson T. A., 2011, ApJ, 735, 66
Navarro J. F., White S. D. M., 1993, MNRAS, 265, 271
Navarro J. F., Frenk C. S., White S. D. M., 1997, ApJ, 490, 493
Pawlik A. H., Schaye J., 2008, MNRAS, 389, 651
Pawlik A. H., Schaye J., 2009, MNRAS, 396, L46
Pawlik A. H., Milosavljević M., Bromm V., 2013, ApJ, 767, 59
Pawlik A. H., Schaye J., Dalla Vecchia C., 2015, preprint (arXiv:1501.01980)
Peebles P. J. E., Yu J. T., 1970, ApJ, 162, 815
Petkova M., Springel V., 2011, MNRAS, 412, 935
Rasera Y., Teyssier R., 2006, A&A, 445, 1
Rees M. J., Ostriker J. P., 1977, MNRAS, 179, 541
Rosdahl J., Teyssier R., 2015, MNRAS, 449, 4380 (R14)
Rosdahl J., Blaizot J., Aubert D., Stranex T., Teyssier R., 2013, MNRAS, 436, 2188 (R13)
Roškar R., Teyssier R., Agertz O., Wetzstein M., Moore B., 2014, MNRAS, 444, 2837
Scannapieco C. et al., 2012, MNRAS, 423, 1726
Schaye J. et al., 2015, MNRAS, 446, 521
Semenov D., Henning T., Helling C., Ilgner M., Sedlmayr E., 2003, A&A, 410, 611
Silk J., 1977, ApJ, 211, 638
Springel V., Di Matteo T., Hernquist L., 2005, MNRAS, 361, 776
Stinson G. S., Brook C., Macciò A. V., Wadsley J., Quinn T. R., Couchman H. M. P., 2013, MNRAS, 428, 129
Strömgren B., 1939, ApJ, 89, 526
Teyssier R., 2002, A&A, 385, 337
Thompson T. A., Quataert E., Murray N., 2005, ApJ, 630, 167
Truelove J. K., Klein R. I., McKee C. F., Holliman J. H., Howell L. H., Greenough J. A., 1997, ApJ, 489, L179
Trujillo-Gomez S., Klypin A., Colín P., Ceverino D., Arraki K. S., Primack J., 2015, MNRAS, 446, 1140
Verner D. A., Ferland G. J., Korista K. T., Yakovlev D. G., 1996, ApJ, 465, 487
White S. D. M., Rees M. J., 1978, MNRAS, 183, 341
Wise J. H., Abel T., 2011, MNRAS, 414, 3458
Wise J. H., Abel T., Turk M. J., Norman M. L., Smith B. D., 2012a, MNRAS, 427, 311
Wise J. H., Turk M. J., Norman M. L., Abel T., 2012b, ApJ, 745, 50
Wise J. H., Demchenko V. G., Halicek M. T., Norman M. L., Turk M. J., Abel T., Smith B. D., 2014, MNRAS, 442, 2560
Zel'dovich Y. B., 1970, A&A, 5, 84

## APPENDIX A: STELLAR LUMINOSITIES AND PHOTON PROPERTIES

The emission from each stellar particle is calculated on the fly for every fine timestep and injected into the host cell, adding to the radiation energy density of all photon groups. For the specific stellar luminosity (i.e. luminosity per unit mass) and photon group properties, we use the SED models of Bruzual & Charlot (2003), where we assume a Chabrier (2003) IMF. The dependence of the specific luminosities and radiation group properties on the stellar population's age and metallicity are shown in Fig. A1. Each photon group's
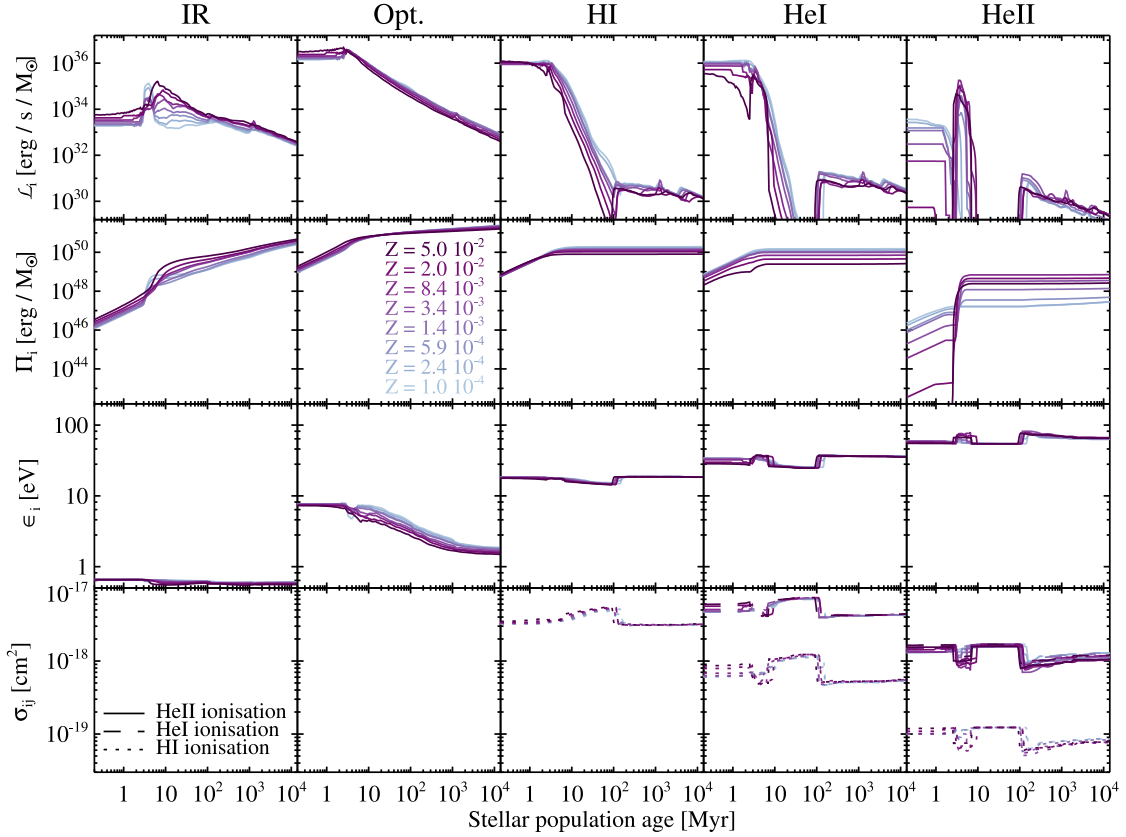
**Figure A1.** Age and metallicity dependence of specific stellar luminosities and photon group attributes derived from the Bruzual & Charlot (2003) SED model, assuming a Chabrier (2003) IMF. The columns represent the five photon groups with increasing photon energy from left to right. Top row: specific luminosity (i.e. luminosity per unit stellar mass), emitted into each photon group from the stellar particles. Second row: cumulative specific luminosity per photon group. Third row: average photon energies. Bottom row: average cross-sections per photoionization interaction. The emission from each stellar particle is calculated on-the-fly in each timestep by integration of the data shown in the second row, given the mass, age and metallicity of the particle. The properties of the five photon groups are updated every five coarse timesteps by a luminosity-weighted average of all existing stellar particles (excluding the stellar particles present in the ICs).

properties (i.e. average energy and cross-section) are updated every five coarse timesteps, using luminosity-weighted averages of the existing stellar particles' emission in the corresponding bands using the frequency-dependent ionization cross-sections from Verner et al. (1996, see also the appendix of R13). This update of the photon groups and the stellar emission is done as detailed in the appendix of R13, except that the specific luminosity is now in terms of emitted energy whereas it was done in terms of photon number count in R13 (which makes more sense in pure ionization calculations). The stellar emission is thus energy-conserving, whereas it was photon number conserving in R13. This difference arises because the spectral shape of an individual stellar particle is not identical to the 'average' shape which is assumed for our photon groups. Due to this difference, one must choose whether the emission is accurate in terms of photon count or energy, and we have chosen energy.

## APPENDIX B: THE REDUCED FLUX APPROXIMATION

In Section 2, we describe the reduced flux approximation, whereby we assume a full reduced flux of photons, $|\boldsymbol{F}| = \tilde{c}E$, when calculating the direct radiation pressure on gas from non-IR photons. The reason for making this approximation is as follows. Radiation is emitted from a stellar particle directly into the cell which hosts the particle, by incrementing the radiation energy density, $E$, while the

photon flux is left unchanged, in accordance with locally isotropic radiation from the stellar population. We use the so-called Global Lax Friedrich Riemann (GLF) solver for the advection of photons between cells (see R13, R14), which has the advantage that radiation is advected isotropically from such sources, i.e. the radiation field retains an isotropic shape, in the limit of a single source and free-streaming radiation. The disadvantage of the GLF solver is that the radiation stays somewhat isotropic inside a buffer of a few cell widths around such a source, i.e. in this region $|\boldsymbol{F}| \ll \tilde{c}E$.

We demonstrate this in Fig. B1, where we show the converged results of a 3D experiment of a single isotropic source of radiation in the middle of a box resolved by $64^3$ cells, and assuming free-streaming radiation, i.e. no interaction between the radiation and the medium. The photons are injected by incrementing $E$ during each timestep, uniformly in the eight cells adjacent to the box centre, according to the luminosity of the source. We plot, as a function of distance $r$ from the source, the analytic expression for the radiation flux, i.e. the 'angle-integrated' flux $\tilde{c}E$, and the magnitude of the photon bulk flux, $|\boldsymbol{F}|$ (pointing away from the source), all in units of $F_0 = \frac{L}{4\pi\Delta x^2}$, where $L$ is the source luminosity and $\Delta x$ the cell width. It can be seen from the plot that $\tilde{c}E$ follows the analytic profile accurately, but within a few $\Delta x$ from the source, $|\boldsymbol{F}| \ll \tilde{c}E$. In solid purple, against the right axis, we plot also the reduced flux of the radiation, $f_\gamma = \frac{|\boldsymbol{F}|}{\tilde{c}E}$. While in reality, one would have $f_\gamma = 1$ at *any* radius for this simple experiment, this is clearly quite far
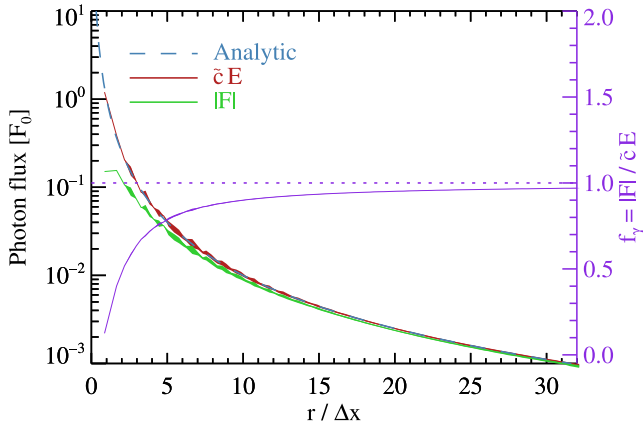
**Figure B1.** Converged results from a simple 3D experiment of a single isotropic source of free-streaming radiation in the centre of a box resolved by $64^3$ cells. We plot the analytic expectation for the $r^{-2}$ radiation flux (dashed blue), the 'angle-integrated' radiation flux, $\tilde{c}E$ (solid red), and the magnitude of the radiation flux away from the source, $|F|$ (solid green), all in units of $F_0$, the expected analytic flux at a distance of one cell width from the source. Against the right axis, in purple, we plot the reduced flux, $f_\gamma$, which is the ratio of $|F|$ and $\tilde{c}E$. The reduced flux curve demonstrates a 'smoothing length' for the reduced flux of a few cell widths around the isotropic radiation source, within which the radiation pressure, $\dot{p}_\gamma \propto F$, is considerably underestimated. The curves for $\tilde{c}E$, $|F|$, and $f_\gamma$ have been binned by radius, and the thickness of the curves reflects the flux range within each radial bin.

from the truth close to the source, with e.g. $f_\gamma(r < 5\Delta x) \lesssim 0.8$. For the advection of photons, photoionization and the associated heating, this is of no consequence, but the *radiation pressure* is correspondingly underestimated in such a buffer of $\approx 5$ cell widths around the source, which can be considered a 'smoothing length' for the radiation pressure $\dot{p}_\gamma \propto F$ (see R14, Section 2.3.3, and equation 27). Typical H II regions in our simulations are badly resolved, which means that most of the ionizing radiation is absorbed within five cell widths from the stellar sources, and hence the direct radiation pressure is potentially underestimated.

We have therefore used the aforementioned reduced flux approximation, renormalizing $F$ to $\tilde{c}E$ for the radiation pressure force in each cell, i.e. assuming a full reduced flux, in the bulk direction of the radiation. As discussed in Section 2, this means we *overestimate* the radiation pressure in two types of locations: (i) in cells hosting stellar radiation sources, where the radiation is in reality isotropic, but we instead take it all to point in the same (average) direction. (ii) In-between radiation sources, where the radiation pressure from opposing fields of radiation would in reality cancel out, but again we instead take it to point in the average direction, which is the direction away from the strongest source. Since we found the effect of direct radiation pressure to be negligible, the use of the reduced flux approximation is conservative and our conclusions are robust.

## APPENDIX C: RESOLUTION TESTS

As is the case with simulation work in general, it is important to investigate the dependence of the results on the numerical resolution. For this reason, we compare runs of the fiducial G9 galaxy with lower resolution counterparts, where the minimum cell width is two times larger and the mass of particles (both formed and in
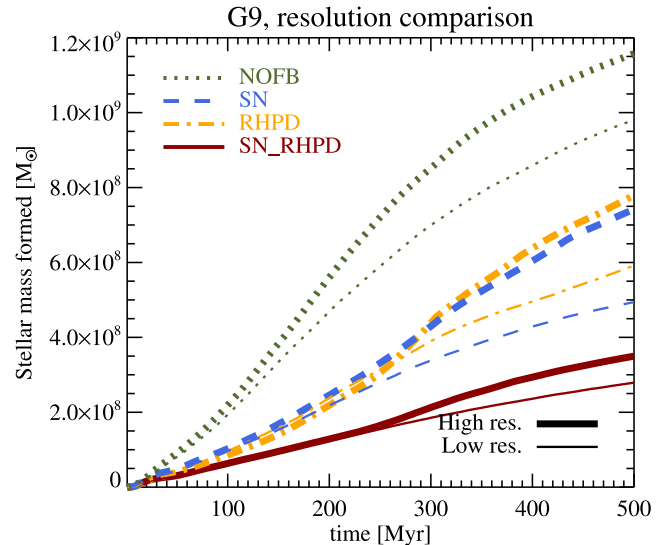


**Figure C1.** Resolution tests. The plot shows comparisons of the stellar mass formed in the G9 galaxy for default (thick curves) and low (thin curves) resolution, for the various feedback models, as indicated in the legend.

the ICs) is eight times larger.[6] Otherwise, the simulation parameters are identical.

Fig. C1 shows the effect of resolution on star formation, with line thickness indicating the resolution (thick for high resolution and thin for low resolution), and as usual the colours and line styles represent different feedback models. We skip here the results from the runs comparing the different radiation processes, i.e. including/excluding direct and reprocessed radiation pressure, and show only the all-inclusive radiation runs, but note that the radiation pressure processes have little and seemingly random effects, i.e. the dominant radiation effect is heating, as we have established in the previous sections.

Lowering the resolution has the effect of reducing the formation of stars, regardless of the feedback process included, even without any feedback. This is a natural outcome of lowering the resolution, since it becomes more difficult for the gas to collapse to high densities, which in turn decreases the star formation rate which scales locally as $\rho^{3/2}$. Indeed, we find the mean densities typically to be higher in the high-resolution runs than in their low-resolution counterparts, by about half a dex. Apart from this systematic suppression in star formation rates with resolution, stellar radiation feedback reduces the formation of stars by roughly a similar fraction: without SN feedback, the addition of radiation feedback reduces the stellar mass formed at 500 Myr by $\approx 40$ per cent. Combined SN and RT feedback results in very similar star formation for the two resolutions, indicating numerical convergence.

In the resolution comparison, it is questionable whether $m_*$ should be changed in the low-resolution simulations. Increasing the stellar particle mass by a factor of 8, as we have done in Fig. C1, can boost the feedback, since each particle then has eight times higher luminosity and SN energy, thus contaminating the pure effect of changing the physical resolution. For the sake of completeness, we thus also ran lower resolution counterparts to the G9 simulations, exactly as just described, but with $m_* = 600\,\mathrm{M}_\odot$, identical to the fiducial simulations, for which the star formation is compared to the higher resolution case in Fig. C2. Here, the effect of SN feedback is

[6] Correspondingly, the IC particles are eight times fewer.
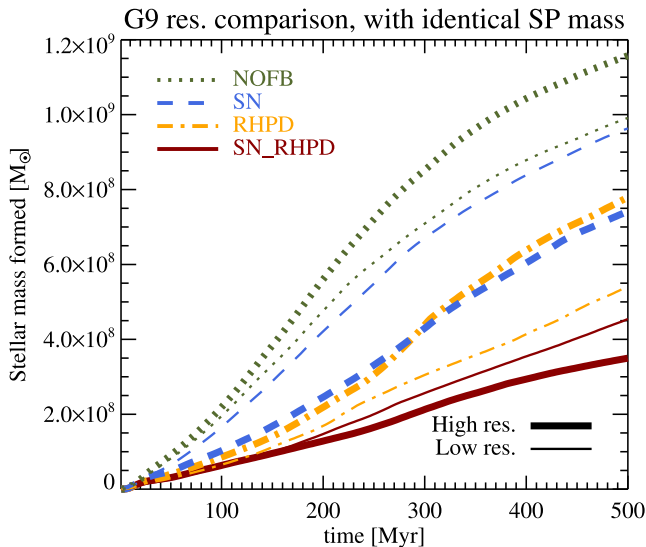
**Figure C2.** Resolution tests with constant stellar particle mass (600 M$_\odot$). The plot shows comparisons of the stellar mass formed in the G9 galaxy for default (thick curves) and low (thin curves) resolution, for the various feedback models, as indicated in the legend.

negligible at low resolution, while pure radiation feedback is *more* efficient than shown in Fig. 4.

## APPENDIX D: REDUCED LIGHT SPEED CONVERGENCE TESTS

To prevent a prohibitively small timestep in our RHD scheme, we use a default reduced light speed of $\tilde{c} = c/200$ in our simulation runs. This is in fact a six times lower light speed than recommended in the analysis of reduced light speeds in ISM simulations in Rosdahl et al. (2013), so it is important to verify that the chosen light speed does not affect our results. For this purpose, we have run the lower resolution equivalent of the G9 galaxy[7] with light speeds six times lower, two times higher, and six times higher than the default value, the last value being recommended by Rosdahl et al. (2013).

In Fig. D1, we plot a comparison of the different light speed runs in the form of the total stellar mass formed during the 500 Myr run time. The light speed has a negligible effect on the star formation. The morphology, outflow rates, and density distributions are also nearly identical in the different light speed runs.

We conclude that our results are well converged in terms of the employed light speed, and we expect that similar results would be retrieved with the full light speed.[8]

While true in the main simulation runs described in this paper, our conclusion on light speed convergence does not necessarily hold when the IR optical depth becomes very high, as in our 'extreme' simulations described in Section 4.3 where we artificially boosted the IR opacity by orders of magnitude compared to the more realistic theoretically motivated value, and found very reduced star

___
[7] Eight times fewer/more massive particles and twice the minimum cell width compared to the default resolution, just as in Appendix C.
[8] Apart from the problem of the computational cost of a run with the full light speed, such a simulation would also likely suffer from HD diffusion with the current setup, due to a large number of very small timesteps. For a full light speed to work with our explicit RT solver, we would need to subcycle the RT within the HD step.
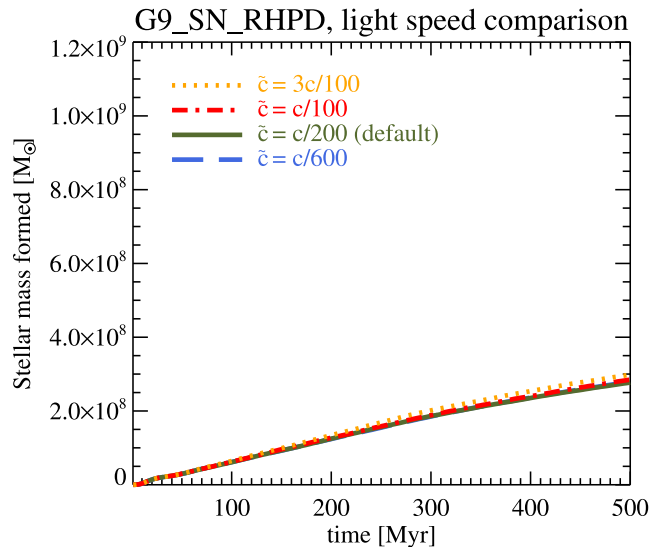
**Figure D1.** Light speed convergence tests. The plot shows comparisons of the stellar mass formed in the G9 lower resolution galaxy (see Appendix C) for the default light speed of $c/200$ (solid green), along with identical runs with the light speed changed by factors of 6, 2, and 1/3, as indicated in the legend.

formation and outflows. When the optical depth becomes very high, the effective propagation speed of radiation scales inversely with the local optical depth, i.e. radiation waves travel at a speed $c/\tau$, where $\tau$ is the optical depth across some relevant length-scale, such as an optically thick cloud (see e.g. sections 2.4 and 3.5 in R14). With our reduced speed of light, radiation waves travel at a speed $\tilde{c}/\tau$, and if $\tilde{c}$ is orders of magnitude smaller than the real light speed, as in this paper, the speed of light can become a severe issue in very optically thick gas, with radiation waves potentially travelling at a speed slower than the gas itself. Since this becomes most severe with the highest optical depths, we ran the most extreme experiment from Section 4.3 ($\tilde{\kappa}_{\rm IR} = 10^4 \, \rm cm^2 \, g^{-1}$) with $\tilde{c}$ increased by a factor 2 and decreased by a factor 3 from the default value, i.e. $\tilde{c} = 10^{-2} \, c$ and $\tilde{c} = 1.67 \times 10^{-3} \, c$, respectively. We found that the average star formation rates are unaffected, but that they fluctuate on a longer time-scale with decreasing light speed, and that outflow rates decrease very substantially with increasing light speed (reinforcing our conclusion that radiation does not produce outflows). It thus appears that with very large optical depth, the reduced speed of light does become an issue for outflows, but not for star formation rates. The main conclusions of this paper are not affected though, since optical depths in our simulations are never very high, save for the extreme 'what if' scenario described in Section 4.3.

This paper has been typeset from a TeX/LaTeX file prepared by the author.